Article
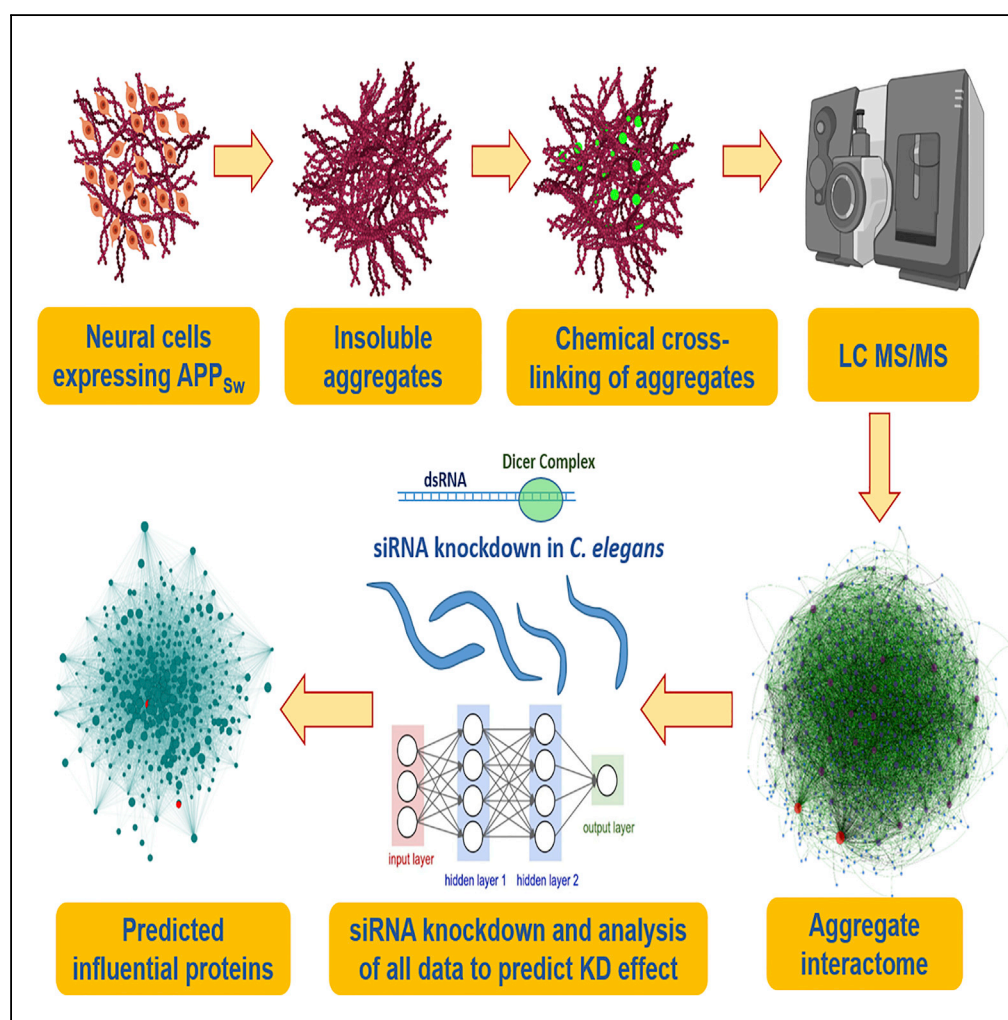
Aggregate Interactome Based on Protein Cross-linking Interfaces Predicts Drug Targets to Limit Aggregation in Neurodegenerative Diseases

Meenakshisundaram Balasubramaniam, Srinivas Ayyadevara, Akshatha Ganne, ..., Peter A. Crooks, Sue T. Griffin, Robert J. Shmookler Reis

mbalasubramaniam@uams.edu (M.B.)
ayyadevarasrinivas@uams.edu (S.A.)
rjsr@uams.edu (R.J.S.R.)

HIGHLIGHTS

Cross-link data support a preferred hierarchy of protein accrual into aggregates

Contact networks can predict proteins that contribute functionally to aggregation

RNAi knockdowns of key hubs and hub connectors imply functional roles in accrual

Aspirin opposes protein aggregation by reducing contactome interactions >5-fold

Article

Aggregate Interactome Based on Protein Cross-linking Interfaces Predicts Drug Targets to Limit Aggregation in Neurodegenerative Diseases

Meenakshisundaram Balasubramaniam,[1,2,*] Srinivas Ayyadevara,[1,2,*] Akshatha Ganne,[3] Samuel Kakraba,[3] Narsimha Reddy Penthala,[4] Xiuxia Du,[5] Peter A. Crooks,[4] Sue T. Griffin,[1,2] and Robert J. Shmookler Reis[1,2,6,*]

SUMMARY

Diagnosis of neurodegenerative diseases hinges on "seed" proteins detected in disease-specific aggregates. These inclusions contain diverse constituents, adhering through aberrant interactions that our prior data indicate are nonrandom. To define preferential protein-protein contacts mediating aggregate coalescence, we created click-chemistry reagents that cross-link neighboring proteins within human, APP$_{Sw}$-driven, neuroblastoma-cell aggregates. These reagents incorporate a biotinyl group to efficiently recover linked tryptic-peptide pairs. Mass-spectroscopy outputs were screened for all possible peptide pairs in the aggregate proteome. These empirical linkages, ranked by abundance, implicate a protein-adherence network termed the "aggregate contactome." Critical hubs and hub-hub interactions were assessed by RNAi-mediated rescue of chemotaxis in aging nematodes, and aggregation-driving properties were inferred by multivariate regression and neural-network approaches. Aspirin, while disrupting aggregation, greatly simplified the aggregate contactome. This approach, and the dynamic model of aggregate accrual it implies, reveals the architecture of insoluble-aggregate networks and may reveal targets susceptible to interventions to ameliorate protein-aggregation diseases.

INTRODUCTION

The presence of specific intra- and extra-cellular aggregates is the hallmark pathology for diverse neurodegenerative diseases, including Alzheimer disease (AD) (Davis et al., 2018). Such aggregates include a wide variety of proteins in addition to the "seed" proteins, i.e., Aβ$_{42}$ and tau in AD, which are believed to initiate the formation of the diagnostic aggregates (Ayyadevara et al., 2016b). Many of these non-seed constituents, including 14-3-3 proteins, chaperones, phosphorylated TDP-43, and neurofilament and motor proteins, are common to a wide variety of pathological aggregates (Ayyadevara et al., 2015, 2016b; David et al., 2010). In previous studies, using *C. elegans* models of neurodegeneration-associated aggregation characteristic of AD and Huntington disease, we identified a wide variety of proteins in aggregates isolated by immuno-pulldown with antibodies to seed proteins. Importantly, many non-seed proteins have key functional roles that would be disrupted by their sequestration into aggregates (Ayyadevara et al., 2015, 2016b, 2016c; Balasubramaniam et al., 2018). In addition, post-translational modifications have been shown to result in structural changes that impact both protein function and aggregation by exposing buried/hydrophobic surfaces to other misfolded proteins (Fink, 1998; Huang et al., 2014; Karve and Cheema, 2011). As an example, we have documented interactions between aggregate proteins that were specific to their phosphorylated forms, e.g., 14-3-3 interactions with hyper-phosphorylated tau (hP-tau), observed only in aggregates from Alzheimer hippocampus (Ayyadevara et al., 2016b).

In the present study, we developed a cross-linking approach to define pathology-associated protein interactions involved in aggregation and to learn how post-synthetic modifications alter those interactions. We developed a two-stage cross-linking protocol that uses click-chemistry to add a high-affinity epitope for enrichment of linked peptide pairs before mass spectrometry. As a proof-of-principle study, we applied this to a cell-culture model of amyloid deposition: human neuroblastoma cells that express an AD-predisposing mutant of APP (SY5Y-APP$_{Sw}$). To identify cross-linked peptides and their phosphorylation state, liquid chromatography-tandem mass spectrometry (LC-MS/MS) data were analyzed by an algorithm targeting peptides previously identified in the aggregate proteome. This strategy allowed us to define the most abundant protein-protein interfaces within aggregates and thus to construct a nonfunctional

[1]McClellan Veterans Medical Ctr., Central Arkansas Veterans Healthcare Service, Little Rock, AR 72205, USA

[2]Department of Geriatrics, Reynolds Institute on Aging, University of Arkansas for Medical Sciences, Little Rock, AR 72205, USA

[3]Bioinformatics Program, University of Arkansas for Medical Sciences, University of Arkansas at Little Rock, Little Rock, AR 72205, USA

[4]Department of Pharmaceutical Sciences, College of Pharmacy, University of Arkansas for Medical Sciences, Little Rock, AR 72205, USA

[5]Department of Bioinformatics & Genomics, University of North Carolina at Charlotte, Charlotte, NC 28223, USA

[6]Lead Contact

*Correspondence:
mbalasubramaniam@uams.edu (M.B.),
ayyadevarasrinivas@uams.edu (S.A.),
rjsr@uams.edu (R.J.S.R.)

https://doi.org/10.1016/j.isci.2019.09.026

interactome, herein termed the "aggregate contactome." Using aspirin as a known positive drug documented to reduce aggregation (Ayyadevara et al., 2013), we then showed that this contactome shrinks after aspirin treatment, due in large part to disappearance of the majority of intra-aggregate interactions. We thus demonstrate that drug candidates and small-molecule libraries can be screened for disruption of key interfaces predicted to mediate the assembly of disease-specific aggregates.

RESULTS
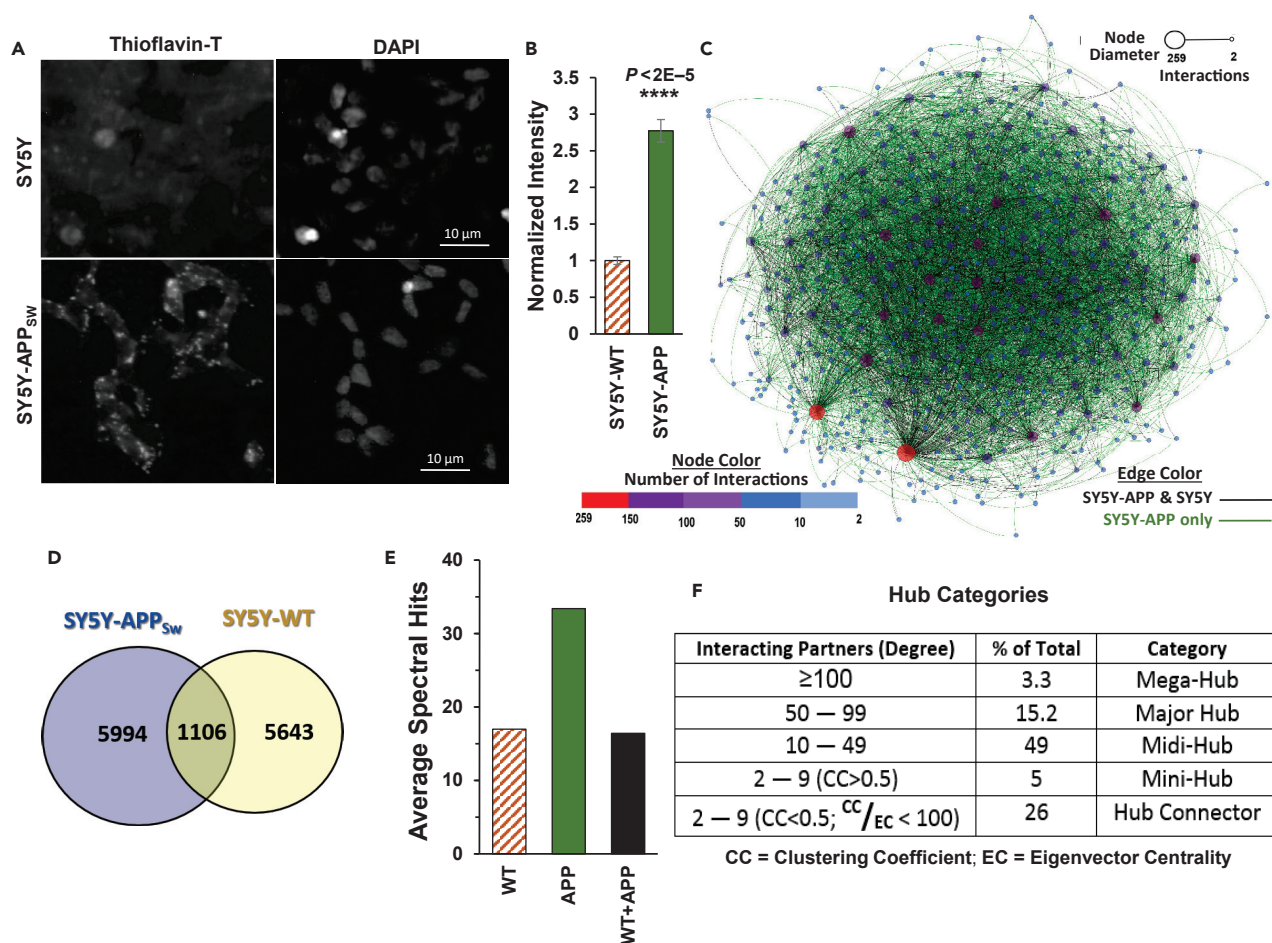
Analysis of Aggregate-Specific Contactomes

To characterize protein:protein contacts within amyloid aggregates, one of the principal diagnostic features of AD, we studied a well-defined model for amyloid accrual, the SY5Y-APP$_{Sw}$ neuroblastoma cell line. These human cells express the "Swedish" dual mutation of Amyloid Precursor Protein (APP$_{Sw}$) observed in familial AD, and unlike their nontransgenic parental cell line SY5Y, they accumulate pericellular amyloid-like aggregates rich in β-pleated sheets (Figure 1A). Although SY5Y cells form a small amount of APP-containing aggregate, these foci are roughly a third as abundant as in SY5Y-APP$_{Sw}$ cells (Figure 1B), based on fluorescence after thioflavin T staining.

To define the aggregate contactome specific to AD-like amyloidosis, sarcosyl-insoluble aggregates were isolated using established protocols (Ayyadevara et al., 2015, 2016b, 2016c) from SY5Y and SY5Y-APP$_{Sw}$ cells. In brief, aggregates were isolated by differential centrifugation before and following addition of 1% sarcosyl, incubated 0.5 h at 22°C with cross-linking reagents, and digested 14 h at 37°C (essentially to completion) with trypsin. A biotin moiety was coupled to the cross-linker by click chemistry (Chowdhury et al., 2009), enabling capture of linked peptide pairs on streptavidin-coated magnetic beads. Eluted peptide pairs were analyzed by high-resolution mass spectrometry, and the raw data files matched to m/z peaks predicted by pairwise addition of masses ([tryptic peptide 1] + linker + [tryptic peptide 2]) within the set of all proteins identified in the same aggregates without cross-linking. Because the latter process is computationally intensive for sets of >500 proteins, we created a multithreading version of Xlink-Identifier (Du et al., 2011) for high-throughput implementation to quantify linked peptide pairs from aggregates (see Supplemental Information, Transparent Methods, for details).

Peptide pairs confirmed as highly abundant in aggregates indicate specific proximal peptides at or near the interfaces of protein:protein interactions. These intra-aggregate cross-links neither exclude nor imply functional interactions between the soluble forms of the same proteins but rather suggest that such adherent surfaces may mediate aggregate accretion. In constructing aggregate contactomes (using GePhi graph-modeling software [Jacomy et al., 2014]), we included only those interactions with ≥10 spectral hits in at least two of three independent cross-linking experiments, thus eliminating protein-protein interfaces that are infrequent or irreproducible. With these constraints, we identified 535 proteins (nodes), comprising 471 unmodified (unphosphorylated) forms and 64 phosphorylated species. Of the 535 nodes, 29 were excluded as non-hub proteins (possessing only one cross-link partner), leaving 506 hubs involved in a total of 7,100 interactions. In Figure 1C, interactions are shown as edges (lines joining hubs), and each hub's color reflects the total number of its interactions to other proteins (see inset keys, Figure 1C).

Comparing hub interaction numbers (first-order connectivity) for aggregates from SY5Y versus SY5Y-APP$_{Sw}$ cells, 5,994 of 7,100 interactions (84.4%) were specific to SY5Y-APP$_{Sw}$, whereas 5,643 of 6,749 (83.6%) were seen only in parental SY5Y cells (Figure 1D). These specific interactions thus depend positively or negatively, respectively, on the presence of mutated APP (APP$_{Sw}$). Although the total number of interactions is quite similar in SY5Y-APP$_{Sw}$ and SY5Y cells, indicating a similar *complexity* of aggregate structure, the average spectral-hit count per linked protein pair unique to SY5Y-APP$_{Sw}$ cells was twice the average for shared or SY5Y-unique pairs (Figure 1E). This abundance ratio is a bit smaller than the ratio estimated from thioflavin T staining (2.7-fold greater intensity for SY5Y-APP$_{Sw}$; Figures 1A and 1B). Thus, the transgenic expression of APP$_{Sw}$ increases the total amount of aggregated protein, but this occurs at the expense of some interactions that had been observed in SY5Y cells lacking APP$_{Sw}$, presumably because key components of those aggregates have been diverted to APP$_{Sw}$-specific aggregates.

The aggregate contactome reveals a complex architecture comprising 506 nodes that vary in degree (number of interacting partners). For each protein node, characteristic descriptors were compiled, including previously reported graph modeling and statistical parameters (Jacomy et al., 2014; Demšar et al., 2013; see Methods for details). As an aid to visualization of candidates and their relative impacts on aggregation,

Figure 1. Analysis of Aggregate-Specific Interactomes

(A) Amyloid-like aggregates were stained with thioflavin T, in SY5Y neuroblastoma cells (top panel) and SY5Y-APP$_{Sw}$ cells (bottom panels). Scale bar indicates 10 μm.

(B) Fluorescence intensity was quantified for cells stained with thioflavin-T; significance was determined by one-tailed t tests. Data are shown as mean ± S.E.M.

(C) Graphical view of the insoluble-aggregate interactome of SY5Y-APP$_{Sw}$ cells. Node (protein) color is based on degree, the number of interacting partners (see key); the edge (interaction) color indicates whether the observed protein-protein contact is peculiar to SY5Y-APP$_{Sw}$ cells (green) or is also present in untransformed ("WT") SY5Y cells (black).

(D) Venn diagram indicating number of interactions that are specific to SY5Y-APP$_{Sw}$ cells, specific to SY5Y, or present in both.

(E) Average spectral hits for observed peptide pairs (total per protein) quantified from SY5Y(WT) and SY5Y-APP$_{Sw}$ cross-linking proteomics. "WT + APP" indicates hits for proteins shared by SY5Y(WT) and SY5Y-APP$_{Sw}$ (see D).

(F) Proteins (nodes) from the aggregate interactome were categorized based on the number of interacting partners (degree), ranging from hub connectors that connect two to nine hub proteins, to mega-hubs ($\geq$100 partners).

hub proteins were partitioned into subcategories of mega, major, midi, and mini hubs based on the abundance of interacting nodes (defined in Figure 1F). Interestingly, the majority of mega-hub proteins ($\geq$100 partners) are either structural or matrix proteins. Roughly half of all aggregate proteins fall into the midi-hub category (10–49 partners), whereas the hub categories just larger and smaller than that comprise 18.5% and 5%, respectively.

We also identified proteins with low levels of direct interaction (<10 partners), connecting higher-degree hubs ($\geq$10 partners) that are not directly associated with one another. For each node in the contactome, we calculated the local, undirected clustering coefficient (CC) as the fraction of triplets (potential node triangles) directly connected to that node, which form closed triangles of three interconnected nodes (Latapy et al., 2008) (see Methods). We also calculated eigenvector centrality (EC, a measure of node

connectivity to high-degree hubs, defined in Methods). Nodes with CC $\leq$ 0.5 and a ratio of EC/CC > k (see Methods) were considered to be influential "hub connectors," which couple to two or more hub proteins that are not directly connected. Hub connectors comprise 134 proteins, or 26.5% of all nodes (Figure 1F).

Cross-link Contactomes Implicate Interactions between APP and Other Proteins

To assess the biological relevance of the cross-link-based contactome, we focused on the interactions of two key seed proteins that are widely accepted as sources of AD aggregate-initiating moieties: APP and tau. AD brain contains both extracellular amyloid plaque (enriched in $A\beta_{42}$, a cleavage product of APP) and intra-neuronal neurofibrillary tangles (containing hP-tau fragments as paired helical filaments, or PHF). These two aggregate types appear at distinct sites in AD tissue; it remains controversial whether either or both drive disease progression and whether there is cross talk between them.

We recently reported evidence of tau:$A\beta_{42}$ interactions within aggregates. Proximity-ligation amplification showed intracellular $A\beta_{42}$ and tau situated within 40 nm of one another, supporting proteomic analyses that identified tau in aggregates purified by $A\beta_{42}$ pulldown and *vice versa* (Ayyadevara et al., 2016b). We are now able to assess whether cross-linking profiles indicate direct or indirect interaction between tau and APP/$A\beta_{42}$. Our analysis of APP interactions (enlarged box in Figure 2A) identified unexpected partners, including SRRM2 and SRSF6_P (pre-mRNA splicing factors), SRRT (miRNA processing component that binds capped primary transcripts), TOP1 (DNA topoisomerase 1), Ki-67 (a DNA-binding marker of cell proliferation), and LAMB2 (laminin B2, which tethers nuclei within the cytoplasm). Ki-67 and laminins were previously implicated in AD as they directly affect aggregation (Gauczynski et al., 2001; Jovanovic et al., 2014; Nagy et al., 1997; Smith and Lippa, 1995). Remarkably, the three largest (highest-degree) hubs among the eight proteins directly cross-linked to APP (SRRM2, SRSF6, and Ki-67) also have first-degree interactions with tau (Figure 2E) or phospho-tau (Figure 2F), implying that they often coalesce in the same aggregates.

APP fragments implicated or enriched in SY5Y-APP$_{Sw}$ aggregates (with $\geq$10 spectral hits and corroborated in at least two independent cross-linking experiments) were mapped back to the intact protein, to define specific sites of all observed APP peptide interactions with other proteins. Surprisingly, all eight APP intra-aggregate interactions involve peptides in the central E2 domain (Lee et al., 2011) (Figure 2B). When we relaxed the threshold to $\geq$3 hits in at least two of three cross-linking experiments, we observed 191 interactions involving peptides within the E2 domain of APP$_{Sw}$ but only six (3.1%) that involve tryptic fragments of the $A\beta_{42}$ peptide. A known limitation of LC-MS/MS proteomics is that not all potential tryptic peptides are equally capable of contributing to identification of a protein; for example, very small or large peptides may never meet the Mascot threshold for high-confidence, unambiguous identification. Because two of the three possible $A\beta_{42}$ peptides were detected abundantly, although in only a few interactions, the observed underrepresentation of $A\beta_{42}$ is unlikely to be artifactual. We note that the two mutations in APP$_{Sw}$ (K595N/M596L) lie adjacent to the β-secretase cleavage site, altering the $A\beta_{42}$/$A\beta_{40}$ ratio and greatly increasing the synthesis of APP itself (Pahrudin Arrozi et al., 2017). They could also have allosteric effects on APP structure elsewhere, similar to distal effects we reported for mutations in the C-terminal region of profilin (Kiaei et al., 2018). Because the E2 domain of APP contains a histidine tetrad with the potential to bind copper or zinc (Dahms et al., 2012), even moderate disturbance of E2 by K595N/M596L could profoundly influence APP's structure and potential for misfolding.

To visually compare observed and predicted interactions within the E2 domain of APP$_{Sw}$, we used HEX protein-protein docking software to model three of the eight observed molecular interactions *in silico*. Such *in silico* simulation results agree well with cross-linking data, providing support for the use of both methods to predict interactions. For example, the ovals in Figures 2C and 2D highlight identified peptide cross-link sites that coincide with computationally predicted protein-protein interfaces between APP$_{Sw}$-E2 and SRRM2 (Figure 2C) or TOP1 (Figure 2D). Similar agreement between peptide cross-linking results and protein docking predictions was also seen for RPS5 (40S ribosomal protein S5; data not shown).

Contactomes Identify Distinct Interacting Partners Specific to Either Unmodified Tau or Hyper-Phosphorylated Tau

Cross-link-based contactomes for tau fragments resolve them into two distinct mini-hubs with differing partners, one for unphosphorylated tau peptides that predominate in normal brain tissue (Figure 2E) and another for phosphorylated peptides (tau-P) typical of hyper-phosphorylated tau (hP-tau; Figure 2F) observed in AD (Ayyadevara et al., 2016b; Simic et al., 2016). Both unmodified tau and hP-tau interactions
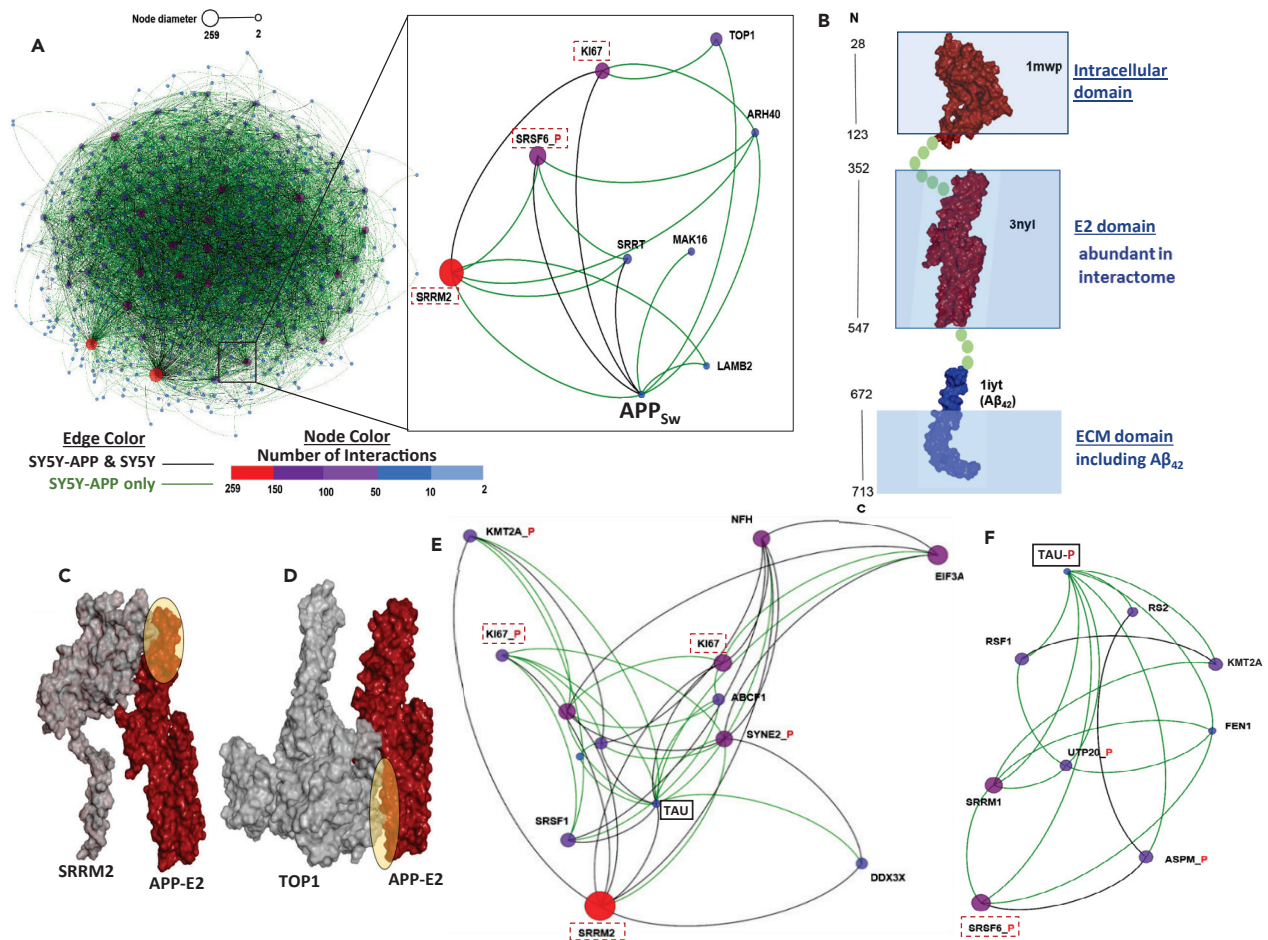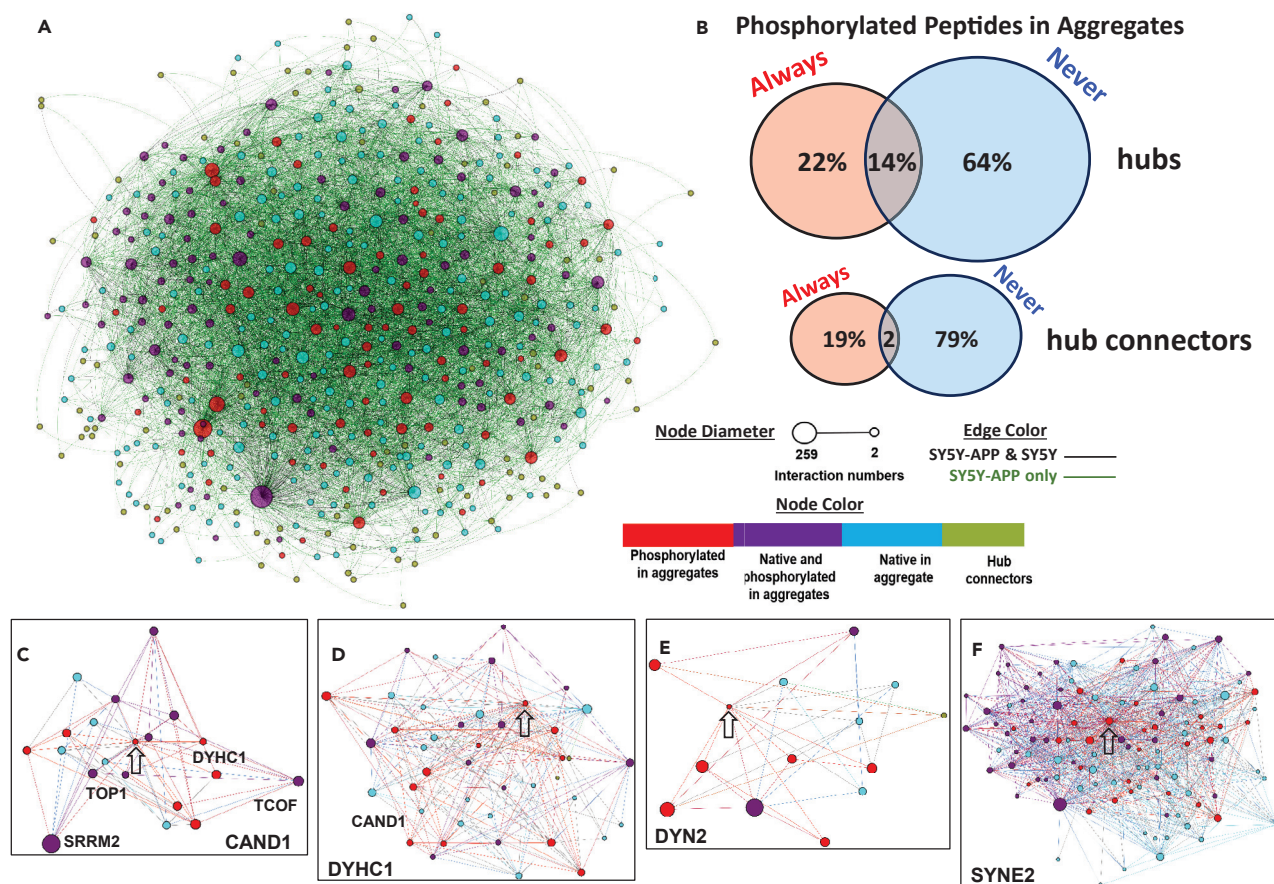
Figure 2. The Aggregate Interactome Identifies Indirect Interactions of APP$_{Sw}$ and Tau

(A) Identified interacting partners of APP (E2 domain) in insoluble SY5Y-APP$_{Sw}$ aggregates.

(B) Domain architecture of APP protein, as inferred from the Protein DataBank (PDB). ECM, extracellular matrix; 1mwp, 3nyl, 1iyt: APP domain IDs in PDB.

(C) Protein-protein docking of SRRM2 and the APP-E2 domain corroborates observed cross-linking data (yellow highlighted area).

(D) Protein-protein docking of TOP1 with APP-E2 corroborates observed cross-linking data (yellow highlighted oval indicates concordant evidence of interaction).

(E) Tau-interacting proteins identified from SY5Y-APP$_{Sw}$ insoluble aggregates. Proteins in dashed boxes also interact with the APP-E2 domain.

(F) Interactions of phosphorylated tau peptides, characteristic of hP-TAU, identified in insoluble aggregates from SY5Y-APP$_{Sw}$. SRSF6_P (dashed box) also interacts with APP-E2.

were found in wild-type SY5Y cells but were far more abundant in SY5Y-APP$_{Sw}$ cells. Remarkably, of 7,255 spectral hits for tau interactions in aggregates (i.e., the sum of spectral hits for two independent isolations of linked-peptide pairs containing a tau or tau-P peptide), none were derived from the PHF region (tau residues 244–378), which is thought to initiate neurofibrillary tangle formation (Fitzpatrick et al., 2017). Our observation that both unmodified and phosphorylated Ki-67 peptides interact directly with unmodified tau fragments (Figure 2E) may help to explain the previously reported critical role of Ki-67 in tau hyperphosphorylation, which in turn leads to the generation of paired helical filaments (Smith and Lippa, 1995).

Protein Phosphorylation in the Aggregate Contactome

Hyperphosphorylation refers to the post-translational addition of multiple phosphate groups. It is typical of several diagnostic seed proteins, including tau, TDP-43, and α-synuclein (Fujiwara et al., 2002; Hasegawa et al., 2008), and is believed to alter protein structure to the detriment of function and stability, while promoting aggregation (Beyer and Ariza, 2013; McFarland et al., 2008; Ren et al., 2007; Rodriguez-Martin et al.,

Figure 3. Protein Phosphorylation in the Aggregate Interactome

(A) Aggregate protein-phosphorylation details inferred from SY5Y-APP_Sw proteomics. Three categories of aggregate proteins were observed: those identified via peptides that are always phosphorylated (red), those with peptides having both phosphorylated and unmodified forms (purple), and those whose peptides are always unmodified (blue). Hub connectors are shown in green.

(B) Venn diagram depicting the composition of aggregate proteins, based on peptide phosphorylation as in (A).

(C) Cross-linked contacts of phosphorylated CAND1 (arrow, cullin-associated and neddylation-dissociated protein 1), showing contactome linkages to other hub proteins, including DYHC1 and mega-hub SRRM2. Of 19 connected hubs, 12 are phosphorylation-state-specific (red or blue).

(D) Cross-linked contacts of phosphorylated DYHC1 (arrow, dynein heavy chain 1), showing that its contactome linkages with other hub proteins are mostly phosphorylation-specific (12 red/always, 17 blue/never, 11 purple/mixed).

(E) Cross-linked contacts of phosphorylated DYN2 (arrow, dynamin 2), showing its contactome linkages with 7 always-phosphorylated/red hub proteins, 4 never-phosphorylated/blue hubs and 2 mixed/purple hubs.

(F) Cross-linked contacts of phosphorylated SYNE2 (arrow, spectrin repeat containing nuclear envelope protein 2) showing complex, mega-hub interactions with other hubs and mega-hubs.

2013). Our cross-linking data distinguish between interactions involving unphosphorylated and phosphorylated peptides within aggregates and thus partition aggregation-associated hub proteins into three categories: 22% of hubs featured peptides that are always phosphorylated (red hubs in Figure 3A), 64% were identified entirely by unmodified peptides (blue hubs), and 14% consisted of mixtures of phosphorylated and unmodified peptides (purple hubs) (Figures 3A and 3B). Among 134 hub connectors, however (green circles in Figure 3A), 19% were exclusively identified through phosphopeptides, 79% entirely via unmodified peptides, and only 2% with both phosphorylated and unmodified peptides (Figure 3B). Scarcity of "ambivalent" hub connectors suggests that they are induced to aggregate by the hubs they connect, rather than through their own misfolding. The observation that 22% of peptides from aggregate-contactome hubs are always phosphorylated, and 36% are at least partially phosphorylated, is consistent with a previous report that phosphopeptides are highly enriched in aggregates (Ayyadevara et al., 2016b) and further implies that sites of abnormal phosphorylation are especially vulnerable to pro-aggregative interactions.

A substantial majority of the aberrantly phosphorylated proteins observed here had been implicated previously in neurodegenerative diseases. For example, CAND1, a component of E3 ubiquitin-ligase complexes, appears only in phosphorylated form in the APP$_{Sw}$ aggregate contactome, allowing us to identify phosphospecific interacting partners (Figure 3C). CAND1 was previously shown to be a PIP$_3$-binding protein that promotes aggregation; its suppression protects several *C. elegans* neurodegeneration models against aggregation and neurotoxicity (Ayyadevara et al., 2016a). Similarly, Dynein Heavy Chain 1 (DYHC1), Dynamin 2 (DYN2), and Nesprin 2 (SYNE2), all previously implicated in neurodegenerative diseases, appear in the aggregate contactome exclusively in phosphorylated forms (Figures 3D–3F).

Contactome Prediction of Critical Hubs for Aggregation Is Supported by Knockdown Effects

We previously showed that many proteins specifically enriched in hippocampal aggregates from patients with AD, relative to age-matched controls, contribute functionally to aggregate growth and progression of pathology in nematode models (Ayyadevara et al., 2016b). For this purpose, we modified two *C. elegans* models of AD-like amyloidosis (kindly provided by C. Link, University of Colorado, Boulder), replacing acute induction of human Aβ$_{42}$ in late development, with leaky (uninduced) expression, so as to better mimic age-progressive amyloid accrual. Strain CL4176, through low-level muscle expression of Aβ$_{42}$, accrues amyloid with age and becomes paralyzed, whereas neuronal Aβ$_{42}$ expression in strain CL2355 progressively disrupts chemotaxis (Ayyadevara et al., 2015, 2016b). Of 21 worm orthologs of AD-enriched aggregate proteins previously targeted by RNAi, 11 were also identified in the SY5Y-APP$_{Sw}$ contactome as key hubs (seven proteins) or hub connectors (four proteins). To this group, we added 25 proteins implicated only by connectivity in the SY5Y-APP$_{Sw}$ aggregate connectome (Figure 4A), for a total of 28 hubs and 8 hub connectors assessed for RNAi rescue of chemotaxis decline. These outputs were used to train a neural network to predict which hub-protein knockdowns would be most effective to reduce aggregation.

Of 36 genes tested, 27 (75%) significantly rescued worms from the chemotaxis decline seen in mock-treated aging controls. Significant rescue was observed after knockdown of genes that encode ankyrin2 (*unc-44*), a neurofilament chain (*mel-28*), clathrin heavy chain (*chc-1*), a splicing factor (SRSF6/*rsp-2*), two DNA helicases (*chd-1*; *ddx-52*), subunits of translation initiation factor EIF3A (*egl-45*) and a DNA replication factor (*rfc-1*), a zinc-finger tumor suppressor (ZN292/*lin-29*), and three heat-shock proteins. Based on chi-squared tests of ratio shifts in individual experiments, significant protection was conferred by RNAi knockdowns targeting 19 of 28 hubs (68%), but 8 of 8 hub connectors (100%). If each proportion is treated as a single point, reducing the comparison to three experimental groups versus three control groups, t tests still indicate that 10 target knockdowns (28%) significantly rescued chemotaxis. To assess whether this high frequency of rescue is peculiar to contactome hubs and hub connectors, 20 RNAi constructs were chosen at random from the Ahringer RNAi library (Kamath and Ahringer, 2003) and knocked down individually in worm groups (Figure S1A). None of these random-RNAi-treated groups differed significantly from simultaneous, mock-treated controls, consistent with our previous experience in which random RNAi targets were only rarely effective in reducing aggregation. This contrast between knockdown of random versus contactome-implicated genes implies that genes encoding hubs and hub connectors are greatly enriched for protective knockdown targets. The protective fractions of hubs (19/28) and hub connectors (8/8) differed from random targets (0/20) with Fisher Exact test p < 3 × 10^{-6} and <4 × 10^{-7}, respectively. Taken together, these data support our hypothesis that the aggregate contactome can identify "non-seed" hub proteins that play key functional roles in aggregate progression and associated neurotoxicity.

Predicting Influential Proteins Based on Contactome Properties of Proteins

Several sequential strategies were combined to predict the functional importance of hubs and hub connectors, as indicated by the chemotactic index (C.I., expressed as fold-change from controls). We first identified 12 primary input variables (predictors) that affect C.I.; these include contactome parameters such as degree (number of direct interacting partners), clustering coefficient (fraction of potential triangles containing a given node as a vertex that are complete), eigenvector centrality (a measure of direct node connections to high-degree nodes); relevant protein descriptors such as molecular weight; and a variety of derived variables including interactions among the primary parameters.

To minimize redundancy (multicollinearity) among input variables, we first used principal-component analysis (PCA), including all 12 input descriptors for each node. PCA indicates that three principal components account for >90% of total C.I. variance (Figure S1B). Considering the variables that underlie each
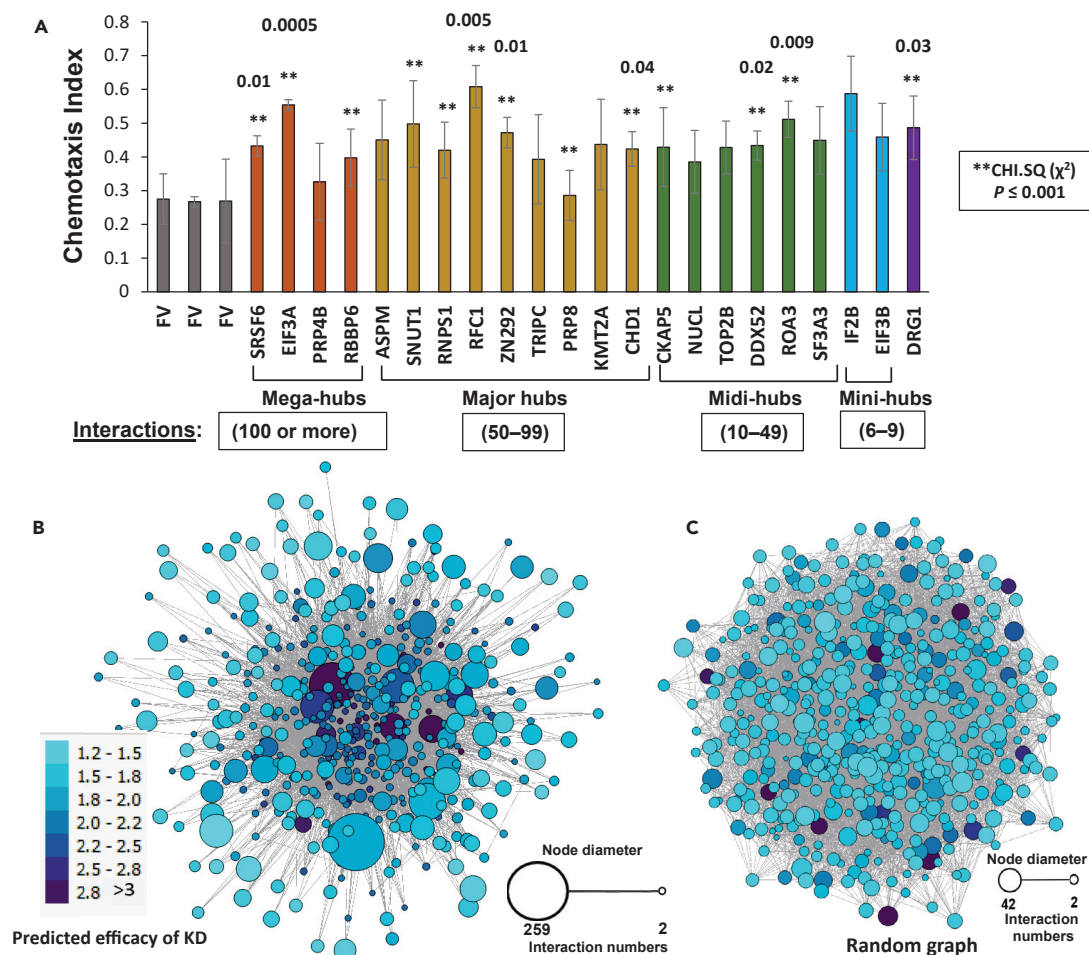
Figure 4. Hub-Protein Knockdown Results Are Consistent with Network-Based Predictions of Hub Centrality and Efficacy

(A) Chemotaxis levels of uninduced *C. elegans* adults (strain CL2355, with pan-neuronal leaky expression of human Aβ$_{42}$), declined to an average chemotaxis index (C.I.) of 0.27 at 5 days of adult age (FV bars). C.I. levels (shown as mean ± S.E.M. for triplicate experiments) are higher for RNAi-treated worms, indicating up to 54% rescue relative to day 1 adult worms (C.I. ≈ 0.9). Knockdown targets were nematode orthologs or homologs of randomly selected human proteins identified in each indicated hub category, from the cross-link-defined contactome of SY5Y-APP$_{Sw}$ neuroblastoma cells. Numbers over bars indicate the unadjusted significance (p values) of hub RNAi knockdowns differing from FV controls, based on heteroscedastic two-tailed paired t tests, considering the C.I. from each of three independent experiments as a single data point. **Unadjusted chi-squared (χ^2) significance of p ≤ 0.001, combined from three independent experiments, i.e., the product of three χ^2 p values comparing treated worms to their simultaneous controls.

(B) Network diagram of the SY5Y-APP$_{Sw}$ contactome, displaying for each hub its degree (number of interactions; see key for node sizes) and the neural network prediction of knockdown efficacy (rescue of chemotaxis as determined in [A]; see key for node colors).

(C) Network diagram of control data, a scale-free network generated with the same node sizes as in (B). In a scale-free network, the degree distribution follows a power law; real-world networks, including protein-protein interaction networks, are widely considered to be scale-free. The distributions of node sizes, edges, and knockdown efficacies are here far more uniform than in the interactome based on empirically observed interactions (B).

component, the number of triangles (X3) alone contributed >90% of the variance explained by principal component 1 (i.e., the predictive value of PC1), clustering coefficient (X4) and molecular weight (X10) together account for >85% of PC2's contribution, and X10 was the predominant contributor to PC3 (45% of its explained variance) (Figure S1C). We next performed stepwise, forward/reverse multivariate linear regression (F/R-MLR), using the PCA-reduced set of variables to identify linear models that provide maximal sensitivity and specificity in predicting the output phenotype. We obtained the most reliable predictions with a model using five inputs: X1/degree, X4/clustering_coefficient, X10/molecular_weight, X1:X4 interactions, and X4:X10 interactions. Virtually identical F/R-MLR results were obtained if X3/triangle_count was substituted for X1/degree; both models gave a Root-Mean-Square Error (RMSE) of 0.25. Although hub degree (number of direct partners, X1) is considered an important variable for the analysis of any network

(Lawyer, 2015), it did not appear in PCA as a major determinant of C.I. This may simply reflect the high correlation between degree (X1) and number of triangles (X3) as illustrated in panel D of Figure S1, since PCA is sensitive to the entry order of redundant input variables. In view of their operational equivalence, the X1-substituted parameter set was carried forward for nonlinear, neural-network optimization.

This sparse set of five inputs was employed to train and test a multi-layer perceptron neural-network algorithm with backpropagation, for the ability to predict knockdown efficacy for each network node. The Orange neural network (Demšar et al., 2013) conducted 50 cycles, in each of which the sample set was randomly partitioned into 70% for training and 30% for testing (see Methods). All hub and hub-connector proteins in the network were thus ranked by the extent of protection predicted for their knockdowns, as listed in Table S1. The contactome plot (Figure 4B), while displaying wide variation in node size, illustrates remarkable clustering or "centrality" of those hubs with the greatest predicted knockdown efficacy. In marked contrast, a control plot generated with the same number of nodes in scale-free mode shows a random distribution of nodes, edges, and degree (interactions/node). Predicted knockdown efficacy (C.I. fold change) is also distributed randomly across the network (Figure 4C), implying that the empirical network derived from cross-linking data (Figure 4B) reflects a distinctly non-random aggregation process. Training and testing the neural network with all 12 initial descriptors (i.e., without dimensional reduction by PCA and MLR modeling) did not improve prediction.

Knockdown of Hub Connectors Is Especially Protective against Chemotaxis Decline

Our initial RNAi screening identified a category of proteins we termed "hub connectors"—hubs of relatively low degree (few direct partners) but high connectivity (many indirect partners, which might otherwise remain unconnected). A formal topological test for this property asks whether a node connects two large hubs without forming a triangle. Hub connectors can thus be defined by two criteria: Clustering Coefficient (CC) < 0.5 and a ratio of CC to Eigenvector Centrality (EC) < 100. On this basis, 135 proteins in the SY5Y-APP$_{Sw}$ aggregate contactome qualify as hub connectors (Figure 1F). Six examples are illustrated as sub-panels of Figure 5A. The 40S ribosomal protein S5 (RPS5 or RS5) is a hub connector linking PPIG (mega-hub) with ATRX (major hub), which do not interact directly. Similarly, hub connector COPG1 (coatomer subunit γ-1) connects midi-hub PHF6 to mega-hubs TITIN and PPIG; and DRG1 (Developmentally Regulated GTP-binding protein 1) links four hub proteins that are otherwise not connected (i.e., the DRG1 triangle count = 0). Actinin 1 and SERF2 are examples of hub connectors that possess triangles but also connect otherwise unconnected hubs (degree > triangles). We reported previously that knockdown of SERF2 in SY5Y-APP$_{Sw}$ cells, or of its ortholog CRAM-1 in C. elegans, confers significant protection against aggregation and associated cytotoxicity (Ayyadevara et al., 2015; Balasubramaniam et al., 2018).

To evaluate their functional importance, five connectome-identified hub connectors were individually suppressed by RNAi in C. elegans strain CL2355. Knockdown of each tested hub connector (RPS5, COPG1, DRG1, ACTN1, and SERF2) conferred significant protection against age-associated aggregation and chemotactic decline in each of three independent experiments (Figure 5B). Hub-connector predictions based on contactome topology are also supported by protein-docking simulations. For example, direct interaction between PPIG and ATRIX is unstable (Figure 5C) but is effectively stabilized when RPS5 serves as a connecting bridge (Figure 5D). Such bridging interactions, which have been largely ignored until now, appear in our analysis to be critical for the growth of pathological aggregates. Moreover, neural-network prediction has revealed many other hub connectors such as HEAT1 and EEF2, which are implicated by our data as key mediators of aggregation (Table S1). Targeting such hub connectors to disrupt their interactions may isolate large-hub clusters and thereby alleviate the aggregate burden.

Aspirin Treatment Reduces Aggregate Complexity

Aspirin (acetylsalicylic acid, or ASA) is an anti-inflammatory acetylating agent that exhibits a wide variety of biological activities (Ayyadevara et al., 2013, 2017; Khaidakov et al., 2010; Stark et al., 2007). In large prospective trials, aspirin reduced or delayed many age-dependent disorders, including neurodegenerative diseases, cardiovascular diseases, and diverse cancers (Jacobs et al., 2012). Its efficacy may be mediated by protection from age-dependent protein aggregation, as we previously demonstrated in several human-cell-culture and C. elegans models of neurodegenerative aggregation (Ayyadevara et al., 2017). For example, amyloid deposits in SY5Y-APP$_{Sw}$ neuroblastoma cells, detected and quantified by fluorescence upon staining with thioflavin T, declined by 27% (p < 0.02) after cells were treated with ASA (Figures 6A and 6B), consistent with our earlier report (Ayyadevara et al., 2017). In view of these and other results supporting ASA antagonism to aggregation, we
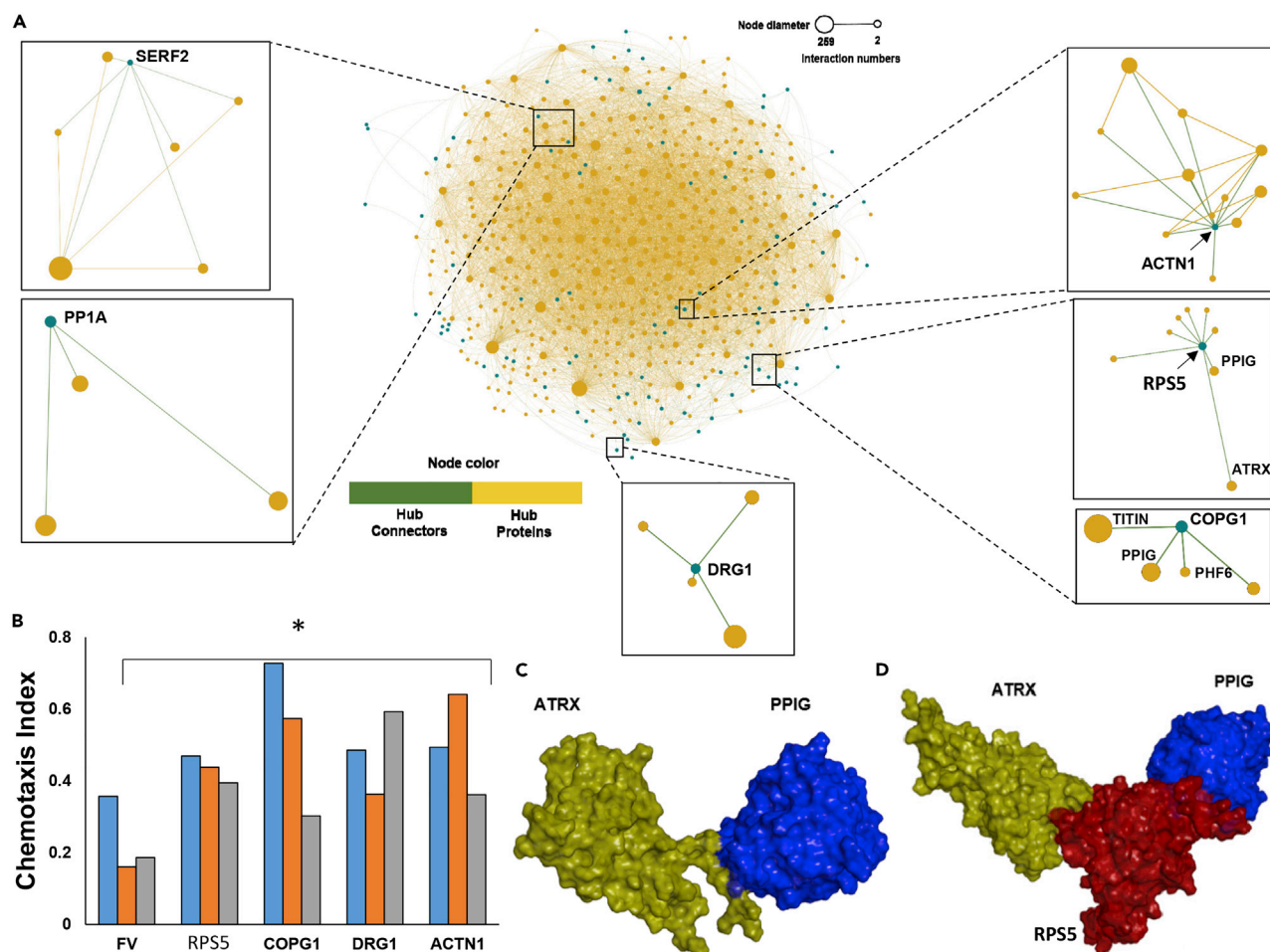
Figure 5. Hub-Connector Knockdowns Rescue Age-Dependent Chemotaxis Decline

(A) SY5Y-APP_Sw interactome showing the distribution of hub connectors (green dots) across the network. Insets show the local contactomes of six hub proteins: SERF2 (small EDRK-rich factor 2 [Balasubramaniam et al., 2018]); PP1A (α catalytic subunit of protein phosphatase 1, PP1, a serine/threonine protein phosphatase involved in cardiac function, learning, and memory); DRG1 (developmentally regulated GTP-binding protein 1, expressed in neural precursor cells); ACTN1 (actinin α1, a cytoskeletal protein related to spectrins and dystrophins); RPS5 (ribosomal protein S5); and COPG1 (coatomer complex subunit γ1, required for budding from Golgi membranes and for retrograde Golgi-to-ER transport of dilysine-tagged proteins).

(B) Rescue of age-dependent chemotaxis loss, by knockdown of hub connectors in *C. elegans* strain CL2355 (uninduced, pan-neuronal Aβ_42 expression). Results are shown for three independent experiments (different-colored bars). *p < 0.04 by one-tailed paired t test, comparing each knockdown to its corresponding, simultaneous FV control.

(C) Computational model of ATRX interacting weakly but directly with PPIG ($\Delta E_{interaction}$ = −73.2 kcal/mol).

(D) Computational model of ATRX interacting strongly with PPIG via the hub connector RPS5 ($\Delta E_{interaction}$ = −120.9 kcal/mol).

constructed the aggregate contactome for aspirin-treated SY5Y-APP_Sw cells (Figure 6C). As is evident from a comparison between Figures 1C and 6C, the aggregate contactome became far sparser and less complex after ASA exposure. The number of protein interactions dropped >2-fold in aspirin-treated cells (Figure 6D), comparable with the >2-fold protection from chemotaxis decline seen in aspirin-treated worms (strain CL2355, with neuronal expression of human Aβ_42; Figure 6E). Aspirin elicited a substantial decline in degree and connectivity of most hub proteins in the SY5Y-APP_Sw contactome, including mega-hubs, consistent with aspirin disrupting aggregation via multiple targets.

Aspirin is a potent acetyl donor, which suggests a plausible mechanism for protection from Aβ aggregation, since we previously showed that Aβ_42 cannot form globular aggregates when acetylated (Ayyadevara et al., 2017). More generally, aggregation is reduced by interventions that favor protein acetylation and promoted by drugs that disrupt acetylation (Ayyadevara et al., 2017). In the SY5Y-APP_Sw aggregate contactome, 84 protein hubs (with two or more interacting partners) were no longer interconnected after aspirin
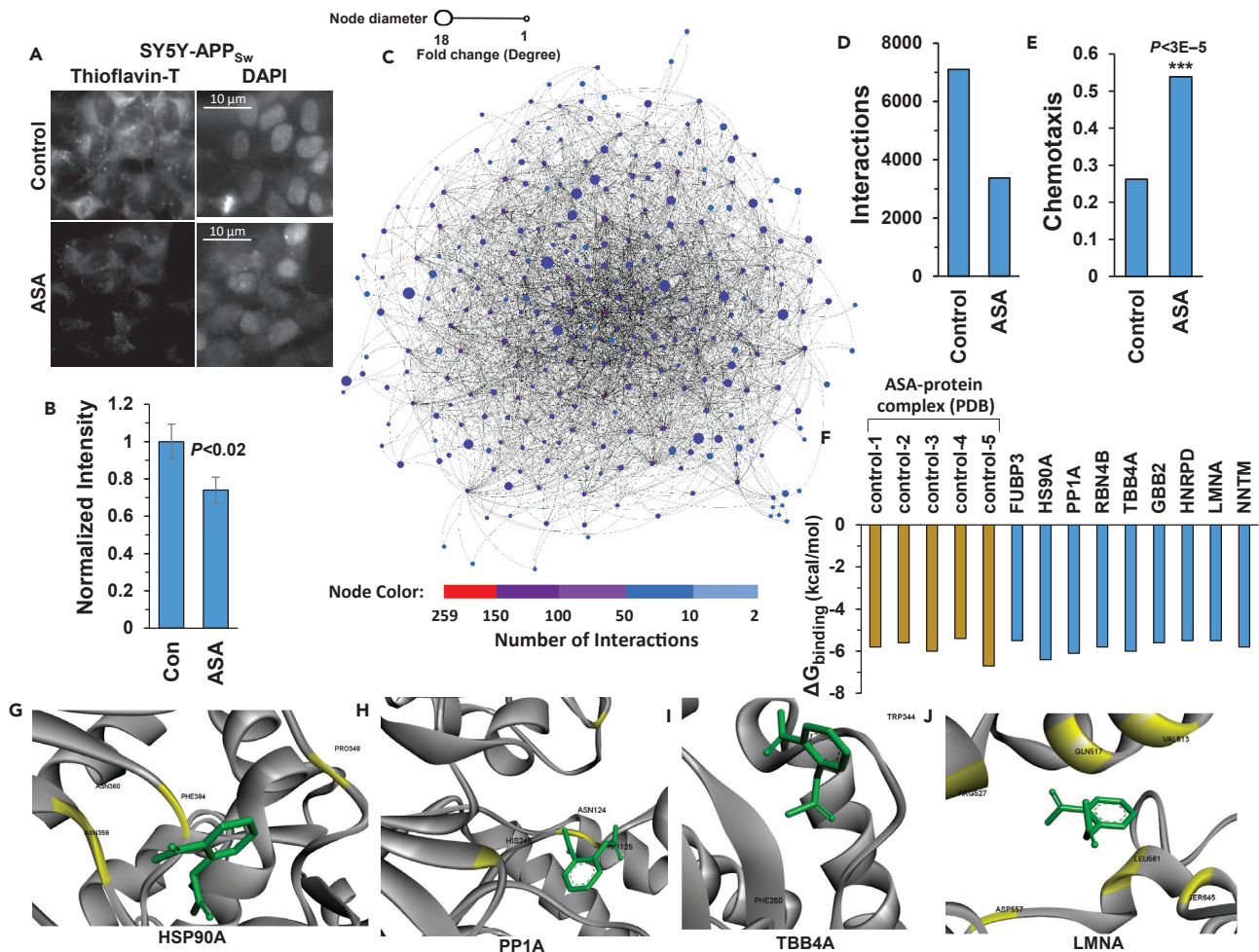
Figure 6. Aspirin Treatment Reduces Aggregate Complexity

(A) Thioflavin-T staining of amyloid in SY5Y-APP$_{Sw}$ cells (images on left), ± simultaneous exposure to 0.5 mM aspirin. DAPI staining of nuclei (images on right) demonstrates similar cell density. Scale bar indicates 10 μm.

(B) Normalized quantitations of amyloid-like aggregation per cell in SY5Y-APP$_{Sw}$ cells, with or without aspirin treatment. Data are shown as mean ± S.E.M. *p < 0.02 by one-tailed t test.

(C) The insoluble-aggregate interactome of SY5Y-APP$_{Sw}$ cells exposed to 0.5 mM aspirin for 48 h shows substantially reduced hub degree and complexity relative to untreated cells (compare with Figure 1C). See also Figure S2.

(D) Number of aggregate-network interactions is reduced by half in SY5Y-APP$_{Sw}$ cells exposed to 0.5 mM aspirin, relative to untreated control cells.

(E) Aspirin (1 mM) protects SY5Y-APP$_{Sw}$ cells against chemotaxis decline in *C. elegans* strain CL2355 (pan-neuronal Aβ$_{42}$ expression) relative to vehicle-only controls. ***p < 2.5 × 10^{-5}, significance by chi-squared (χ^2) test.

(F) Interaction energies (ΔG$_{binding}$) predicted by computational docking of aspirin with candidate proteins (blue bars, network-implicated hub proteins) versus previously reported ASA-binding targets (tan bars, five positive controls to confirm correct docking parameters).

(G–J) Aspirin docking poses of proteins predicted to be direct ASA-binding targets (Ayyadevara et al., 2017): (G) HSP90A (heat shock protein 90α); (H) PP1A (see Figure 5A legend); (I) TUBB4A (tubulin beta chain 4A, a major constituent of microtubules); and (J) LMNA (lamin 4 A/C, a constituent of nuclear lamina; mutations are implicated in several muscular and cardiac dystrophies and in Hutchinson-Gilford progeria).

treatment. Among the proteins that aspirin treatment rendered noninteractive, a substantial number had been previously implicated in neurodegenerative diseases, e.g., ROA3, SERF2, COF2, TBB4A, TBB4B, phosphorylated forms of HSP90α, LMNA, RS11, and protein phosphatase PP1A (a "hub-connector") (Blair et al., 2014; Jovanovic et al., 2014; Martin et al., 2014; Salama et al., 2018).

In recent studies, aspirin-binding regions were identified in a number of ASA-target proteins, including phospholipases (Dai et al., 2016; Singh et al., 2005). This suggested that aspirin might also interact directly with some of the proteins that vanished from the aggregate contactome of aspirin-treated cells. We

selected five protein-aspirin complexes with structures resolved experimentally and documented in Protein DataBank (PDB; www.rcsb.org) as positive examples to validate parameters for computational docking and modeled 19 protein structures. Under the same standard conditions that replicated known aspirin binding to all five positive-control proteins, protein-ligand docking predicted direct, stable aspirin binding to 9 of the 19 tested proteins removed from the contactome by ASA: FUBP3, HSP90A, PP1A, RBN4B, TBB4A, GBB2, HNRPD, LMNA, and NNTM (Figures 6F–6J). The predicted stability of aspirin binding was similar for these nine proteins (blue bars in Figure 6F) and the five positive controls (tan bars), such that the $\Delta G_{binding}$ ranges are almost identical. It is noteworthy that HSP90A phosphorylation, which has been implicated in AD (Blair et al., 2014), is predicted to be blocked by ASA (Figure 6G). Likewise, phosphorylated forms of LMNA are also missing from the aspirin-treated contactome, suggesting that aspirin binding may inhibit phosphorylation and thus block LMNA entry into the contactome. These data highlight the importance of post-translational modification—in particular phosphorylation and acetylation—in aggregate accrual, and suggest that aspirin and other therapeutic drugs may prevent or slow aggregate accumulation and its associated neurotoxicity.

We repeated the above-mentioned contactome analyses after restricting consideration to only those aggregate-protein interactions shared by SY5Y-APP$_{Sw}$ and SY5Y cells (Figure S2). Results were essentially unchanged, with aspirin treatment reducing the number and connectivity (degree) of hubs by > 5-fold for this subset of confirmed interactions.

DISCUSSION

We have developed tools, and an integrated strategy, that enabled us to define the molecular interfaces formed in the accrual of insoluble protein aggregates. This approach comprised the design and synthesis of click reagents for efficient cross-linking and recovery of proximal peptides within aggregates, analysis of cross-linked peptide pairs by LC-MS/MS, and the development and application of improved bioinformatics tools to identify cross-linked peptides. The resulting data were used to construct nonfunctional interactomes ("contactomes") that define the internal architecture of aggregates from SY5Y-APP$_{Sw}$, human neuronal cells expressing AD-prone mutations of Amyloid Precursor Protein.

In previous studies, we identified and quantified constituent proteins that are enriched in aggregates from AD-affected human hippocampus, relative to controls, and demonstrated functional roles for many of these proteins by RNAi knockdown of orthologous genes in *C. elegans* models of AD and other neurodegenerative diseases (Ayyadevara et al., 2016b). Significant protection against aggregation was observed upon knockdown of many aggregate-resident proteins, extending well beyond the known seed proteins thought to initiate aggregation (Aβ$_{42}$ and tau for AD, α-synuclein for Parkinson disease, and huntingtin protein with expanded polyglutamine tracts for Huntington Disease) (Ayyadevara et al., 2015; Ayyadevara et al., 2016b). These results implied that many additional proteins play functional roles in aggregate initiation and/or progression. It remained uncertain, however, what those roles are and how diverse aggregate proteins coalesce into insoluble complexes.

Not all protein pairs can interact to form a stable interface, but a remarkably large fraction of those that do contribute causally to aggregate accrual (i.e., their knockdowns relieve aggregation), leading us to postulate that there is a preferred order of accretions. To elucidate this process, we analyzed cross-linked peptides to define the most abundant protein-protein interfaces in aggregates and thus to construct aggregate-interaction networks. The resulting contactomes reflect only peptide proximity at protein-protein interfaces or adhesion sites rather than functional interactions. Because the contactome is based on semi-quantitative data from cross-linking of aggregates that are likely to be heterogeneous within each cell and between cells, we set abundance thresholds to eliminate rarer interactions and also separated proteins into hub categories (mini-, midi-, major, and mega-hubs), bins that reflect the number of directly interacting partners for each hub. This analysis identified proteins that are predicted to strongly affect aggregate size and stability, owing to high abundance and diversity of either direct contacts (degree) or indirect partners (connectivity). Table S1 lists parameters that best predicted the extent of RNAi rescue from aggregation-mediated pathology. Neural-network predictions from these features correlated quite well (R = 0.77) with observed rescue efficacies.

Within the cross-link-based interactome, mega-hubs (nodes with ≥ 100 partners) include many proteins that bind DNA or RNA (enrichment p < 2E−20 and p < 3E−150, respectively). High cross-link frequencies

were also observed for large structural proteins (e.g., TITIN, SRRM2, SRSF6), which because of their massive size yield large numbers of tryptic peptides with the potential to appear in cross-linked peptide pairs. These large macromolecules should not be discounted, however, since they are often components of intracellular structures such as microtubules and actin filaments, which may provide potent nexi of aggregate accrual upon partial denaturation.

In a model system with high propensity for amyloid aggregation (SY5Y-APP$_{Sw}$ cells), but not in the nontransgenic parental cell line SY5Y, the aggregate contactome shows APP proximity to laminin B2 (Figure 2A). Integrins normally anchor cells to laminins of the extracellular matrix (ECM), and both protein families have been previously implicated in several neurological disorders (Sethi and Zaia, 2017). Kainic acid induces excitotoxicity, leading to laminin degradation, neuronal loss, and eventual degeneration of hippocampal neurons (Bonneh-Barkay and Wiley, 2009). Laminin B2, by interacting with APP, may alter its interactions to other proteins, dislodging cells from their normal ECM anchoring.

Hyperphosphorylated tau (hP-tau, with phosphorylated sites typical of AD) also shows many interactions specific to the SY5Y-APP$_{Sw}$ transgenic cell line (Figure 2F), which differ strikingly from the connectome of tau carrying only normal phosphorylations within the same cells (Figure 2E). Curiously, the contactome derived from SY5Y-APP$_{Sw}$ aggregates includes no peptides from the PHF region, widely believed to initiate tau seeding of neurofibrillary tangles (Fitzpatrick et al., 2017). It is noteworthy that all interactions of AD-like hP-tau, seen in SY5Y-APP$_{Sw}$ cells but not in SY5Y, were lost upon exposure to aspirin (Figure 6).

Of the proteins identified in SY5Y-APP$_{Sw}$ aggregates, 26% are disordered (e.g., 14-3-3, ROA3, SERF2), drawn from all hub categories, but chiefly midi-hubs, major hubs, and hub connectors. Being largely disordered or unstructured, these proteins can adopt multiple conformations and interact with multiple protein partners, making them difficult to target by structure-based drug design. Nevertheless, disordered proteins may adopt stable conformations when bound to other proteins (Ayyadevara et al., 2015; Balasubramaniam et al., 2018; Hu et al., 2014). Protein-protein interaction inhibitors (PPIIs), in particular those that target specific protein interfaces, have received considerable attention as potential therapeutic drugs for neurodegenerative and other diseases (Jnoff et al., 2014; Petta et al., 2016). Preferred interacting partners of disordered proteins, identified by aggregate cross-linking, may reveal stable or meta-stable conformations of these proteins within such complexes, which can be targeted by PPIIs.

We previously identified post-translationally modified (phosphorylated) proteins that are highly enriched in Alzheimer brain aggregates, using standard proteomic methods (Ayyadevara et al., 2016b). The present study corroborates many of those observations in a cell culture model of AD-like amyloid formation and demonstrates that key aggregate proteins adhere to different partners when phosphorylated. Key contactome hubs and hub connectors include proteins previously implicated in neurodegenerative diseases, such as HSP90 (vulnerable to phosphorylation and implicated in AD [Blair et al., 2014]). HSP90 was identified in insoluble AD aggregates, especially in the phosphorylated form, interacting with a variety of proteins (Ayyadevara et al., 2016b). Interestingly, aspirin treatment of SY5Y-APP$_{Sw}$ cells removed HSP90 from the interactome. Small-molecule docking simulations indicate that aspirin could directly bind to HSP90, which is especially intriguing in view of prior reports that ATPase inhibition of HSP90 reduces tau aggregation (Blair et al., 2014).

Knockdowns in *C. elegans*, of orthologs or homologs of human proteins in each hub category from the aggregate contactome, demonstrated their functional roles in aggregate progression and maintenance. Network analyses of SY5Y-APP$_{Sw}$ aggregates specify a variety of node descriptors, including degree and eigenvector centrality, for all nodes identified in the contactome. Because the dependent variable used for machine learning (fold protection against chemotaxis loss) was based on empirical data quantifying a behavioral consequence of amyloid deposition, and its relief by an intervention (RNAi-mediated knockdown), these neural-network predictions provide an unexplored approach to the future development of PPII interventions.

The cross-link-based aggregate contactome identifies peptide pairs within or adjacent to sites of dysfunctional protein-protein adhesion, creating intriguing opportunities for intervention. PPIIs targeting such interfaces might block key aggregation steps without affecting normal protein functions, whereas drugs

targeting active sites or cofactor-binding sites are likely to inhibit the normal functions of their target proteins and also of structurally homologous "off-target" protein sites that bind the same or similar ligands.

Hub connectors constitute an interesting category in contactome analysis. Although hub proteins can augment aggregate networks in proportion to the abundance of hub-interacting partners, their coalescence into large, autophagy-resistant aggregates presumably requires linkage among hubs. Hub connectors can allow otherwise isolated hubs to interact indirectly with large assemblies of inter-connected hubs (Figure 5). Owing to the paucity of direct partners, hub connectors and their interfaces with large hubs may be valuable targets for drugs, which may have lower toxicity than molecules targeting mega-hubs (Agarwal et al., 2010), while at the same time achieving high efficacy owing to disruption of the assembly of large aggregates resistant to degradation via autophagy.

Only a small subset of protein pairs interact to form stable protein-protein interfaces, but a remarkably large fraction of those that do contribute causally to aggregate accrual (i.e., based on our data 77% of their knockdowns relieve aggregation). This surprising result led us to postulate that there is a preferred order of protein-protein interfaces/accretions, which can be interrupted at multiple steps. By identifying cross-linked peptides, we enumerated the most abundant protein-protein interfaces in an aggregate, enabling us to construct aggregate-interaction networks. The resulting protein-protein contactomes reflect only peptide proximity at protein-protein adhesion sites, rather than functional interactions. Because the contactome is based on semi-quantitative data from cross-linking of aggregates that are likely to be heterogeneous within each cell and between cells, we set stringent abundance and replication thresholds to eliminate rarer interactions. Our analysis identified proteins that are predicted to be strong determinants of aggregate size and stability, owing to their high abundance and diversity of either direct or indirect connections.

Numerous reports have identified anti-aggregation effects of aspirin (Ayyadevara et al., 2013, 2017; Moafian et al., 2016). Acetylation of proteins may, in a site-specific manner, alter protein structure. These altered structures may be either predisposed or resistant to aggregation, with resistance more likely if the acetylated residue would otherwise be a target for hyperphosphorylation (Ayyadevara et al., 2017). Aspirin treatment was protective in several *C. elegans* models of neurodegenerative aggregation (Ayyadevara et al., 2017), but little is known about its targets or mechanism of protection. A comparison of cross-link-based aggregate contactomes (Figures 1C versus 6C) demonstrates that aspirin exposure reduces interaction frequency and complexity. Moreover, 84 proteins were removed from the contactome by aspirin exposure, and molecular-dynamic modeling presented here supports the likelihood that they are aspirin targets. Of these 84 proteins, 26 were phosphorylated in untreated SY5Y-APP$_{Sw}$ cells but not in aspirin-exposed cells. Aspirin could block phosphorylation in several ways: by interacting with kinase-targeted sites of these proteins (by either binding or acetylating them) or by similar interactions disrupting upstream kinases that are required to phosphorylate such proteins.

The approach described here defines the physical contactome of AD-like aggregates and thus the local affinities of proximal protein regions. Many aggregate components had never previously been implicated in neurodegeneration, and many interactions are specific to cells expressing the APP$_{Sw}$ protein thought to foster seeding of AD-associated amyloid deposits. Identification of protein pairs that contribute disproportionately to aggregation may reveal attractive targets for interface-binding drugs to oppose protein aggregation. The strategies described here should also be quite generally applicable to the wide variety of neuropathies and other aging-associated diseases that feature progressive protein aggregation.

Limitations of the Study

Use of a neuronal cell culture predisposed to amyloid deposition provides a partial model of AD but is here intended as a well-controlled source of aggregates to validate our protocol. Cross-linking results from AD and control aggregates will be presented elsewhere.

Recovery of peptides from aggregates depends on the ability of trypsin to digest coalesced proteins. We reasoned that protease digestion should progressively degrade aggregates and tested this premise initially with Q40::YFP seeded by, and largely comprising, Q40::YFP (expressed in muscle of *C. elegans* strain AM141), isolated by YFP pulldown. Within 15–30 min of tryptic digestion under our standard conditions, YFP fluorescence declined to ~12% of the control level, implying that as much as 12% of aggregates

may be trypsin resistant. Similarly, sarcosyl-insoluble aggregates from AD hippocampus indicated ~6% resistance to tryptic digestion, based on material failing to enter an electrophoretic gel. Such material will not be included in analyses conducted under the present protocol, although we note that Proteinase K digestion under denaturing conditions, 2% SDS at 65°C, leaves no residual aggregate protein (<0.1% undigested).

In addition, cross-linking of aggregate proteins depends on penetration of the cross-linking reagents, which may limit the representation of cross-linked peptides from aggregate interiors. We anticipated that cross-linking would quench YFP fluorescence in Q40::YFP aggregates from AM141, and indeed fluorescent emissions from mature aggregates were reduced to <1% of the control level within 30 min. We note that the click reagents we employed are much smaller than trypsin, which may account for their superior penetrance.

One additional caveat is that the bioinformatics procedure for identification of cross-linked peptide pairs (Xlink-Identifier; Du et al., 2011) is entirely dependent on the availability of a reference list of proteins and their post-translational modifications, identified in uncross-linked aggregates. Peptides from proteins not represented in this lookup table, including any isoforms not present or any PTMs not identified, cannot be detected by the software. It should also be noted that analysis requires high-resolution mass spectrometry outputs and may be quite computationally demanding for large reference lists.

METHODS

All methods can be found in the accompanying Transparent Methods supplemental file.

DATA AND CODE AVAILABILITY

The link (database: accession number) for our raw data file reported in this paper, comprising all detected matches to predicted m/z values of linked peptide pairs, is Mendeley: http://dx.doi.org/10.17632/pw92vvj9rz.1#folder-d89b63a4-2d13-4eac-85af-cc082696412f

SUPPLEMENTAL INFORMATION

Supplemental Information can be found online at https://doi.org/10.1016/j.isci.2019.09.026.

AUTHOR CONTRIBUTIONS

R.J.S.R., S.A., and M.B. planned and designed the study; N.R.P. synthesized cross-linker and biotin-azide reagents with guidance from P.A.C.; A.G. performed three-dimensional modeling of proteins; S.K. performed PCA, MLR, and statistical modeling of the contactome; X.D. provided the primary scripts for Xlink-Identifier; M.B. performed cross-linking, network modeling, RNAi knockdown, machine learning/neural network algorithms, and other experiments mentioned in the article. R.J.S.R. and M.B. wrote the manuscript with contributions from S.T.G., S.A., and P.A.C.

DECLARATION OF INTERESTS

The authors declare no competing interests.

iScience

CellPress

REFERENCES

Agarwal, S., Deane, C.M., Porter, M.A., and Jones, N.S. (2010). Revisiting date and party hubs: novel approaches to role assignment in protein interaction networks. PLoS Comput. Biol. *6*, e1000817.

Ayyadevara, S., Bharill, P., Dandapat, A., Hu, C., Khaidakov, M., Mitra, S., Shmookler Reis, R.J., and Mehta, J.L. (2013). Aspirin inhibits oxidant stress, reduces age-associated functional declines, and extends lifespan of *Caenorhabditis elegans*. Antioxid. Redox Signal. *18*, 481–490.

Ayyadevara, S., Balasubramaniam, M., Gao, Y., Yu, L.R., Alla, R., and Shmookler Reis, R.J. (2015). Proteins in aggregates functionally impact multiple neurodegenerative disease models by forming proteasome-blocking complexes. Aging Cell *14*, 35–48.

Ayyadevara, S., Balasubramaniam, M., Johnson, J., Alla, R., Mackintosh, S.G., and Shmookler Reis, R.J. (2016a). PIP$_3$-binding proteins promote age-dependent protein aggregation and limit survival in *C. elegans*. Oncotarget *7*, 48870–48886.

Ayyadevara, S., Balasubramaniam, M., Parcon, P.A., Barger, S.W., Griffin, W.S., Alla, R., Tackett, A.J., Mackintosh, S.G., Petricoin, E., Zhou, W., et al. (2016b). Proteins that mediate protein aggregation and cytotoxicity distinguish Alzheimer's hippocampus from normal controls. Aging Cell *15*, 924–939.

Ayyadevara, S., Mercanti, F., Wang, X., Mackintosh, S.G., Tackett, A.J., Prayaga, S.V., Romeo, F., Shmookler Reis, R.J., and Mehta, J.L. (2016c). Age- and hypertension-associated protein aggregates in mouse heart have similar proteomic profiles. Hypertension *67*, 1006–1013.

Ayyadevara, S., Balasubramaniam, M., Kakraba, S., Alla, R., Mehta, J.L., and Shmookler Reis, R.J. (2017). Aspirin-mediated acetylation protects against multiple neurodegenerative pathologies by impeding protein aggregation. Antioxid. Redox Signal. *27*, 1383–1396.

Balasubramaniam, M., Ayyadevara, S., and Shmookler Reis, R.J. (2018). Structural insights into pro-aggregation effects of *C. elegans* CRAM-1 and its human ortholog SERF2. Sci. Rep. *8*, 14891.

Beyer, K., and Ariza, A. (2013). alpha-Synuclein posttranslational modification and alternative splicing as a trigger for neurodegeneration. Mol. Neurobiol. *47*, 509–524.

Blair, L.J., Sabbagh, J.J., and Dickey, C.A. (2014). Targeting Hsp90 and its co-chaperones to treat Alzheimer's disease. Expert Opin. Ther. Targets *18*, 1219–1232.

Bonneh-Barkay, D., and Wiley, C.A. (2009). Brain extracellular matrix in neurodegeneration. Brain Pathol. *19*, 573–585.

Chowdhury, S.M., Du, X., Tolic, N., Wu, S., Moore, R.J., Mayer, M.U., Smith, R.D., and Adkins, J.N. (2009). Identification of cross-linked peptides after click-based enrichment using sequential collision-induced dissociation and electron transfer dissociation tandem mass spectrometry. Anal. Chem. *81*, 5524–5532.

Dahms, S.O., Konnig, I., Roeser, D., Guhrs, K.H., Mayer, M.C., Kaden, D., Multhaup, G., and Than, M.E. (2012). Metal binding dictates conformation and function of the amyloid precursor protein (APP) E2 domain. J. Mol. Biol. *416*, 438–452.

Dai, S.X., Li, W.X., Li, G.H., and Huang, J.F. (2016). Proteome-wide prediction of targets for aspirin: new insight into the molecular mechanism of aspirin. Peer J. *4*, e1791.

David, D.C., Ollikainen, N., Trinidad, J.C., Cary, M.P., Burlingame, A.L., and Kenyon, C. (2010). Widespread protein aggregation as an inherent part of aging in *C. elegans*. PLoS Biol. *8*, e1000450.

Davis, A.A., Leyns, C.E.G., and Holtzman, D.M. (2018). Intercellular spread of protein aggregates in neurodegenerative disease. Annu. Rev. Cell Dev. Biol. *34*, 545–568.

Demšar, U., Harris, P., Brunsdon, C., Stewart Fotheringham, A., and McLoone, S. (2013). Principal component analysis on spatial data: an overview. Ann. Assoc. Am. Geogr. *103*, 106–128.

Du, X., Chowdhury, S.M., Manes, N.P., Wu, S., Mayer, M.U., Adkins, J.N., Anderson, G.A., and Smith, R.D. (2011). Xlink-Identifier: an automated data analysis platform for confident identifications of chemically cross-linked peptides using tandem mass spectrometry. J. Proteome Res. *10*, 923–931.

Fink, A.L. (1998). Protein aggregation: folding aggregates, inclusion bodies and amyloid. Fold. Des. *3*, R9–R23.

Fitzpatrick, A.W.P., Falcon, B., He, S., Murzin, A.G., Murshudov, G., Garringer, H.J., Crowther, R.A., Ghetti, B., Goedert, M., and Scheres, S.H.W. (2017). Cryo-EM structures of tau filaments from Alzheimer's disease. Nature *547*, 185–190.

Fujiwara, H., Hasegawa, M., Dohmae, N., Kawashima, A., Masliah, E., Goldberg, M.S., Shen, J., Takio, K., and Iwatsubo, T. (2002). alpha-Synuclein is phosphorylated in synucleinopathy lesions. Nat. Cell Biol. *4*, 160–164.

Gauczynski, S., Peyrin, J.M., Haik, S., Leucht, C., Hundt, C., Rieger, R., Krasemann, S., Deslys, J.P., Dormont, D., Lasmezas, C.I., et al. (2001). The 37-kDa/67-kDa laminin receptor acts as the cell-surface receptor for the cellular prion protein. EMBO J. *20*, 5863–5875.

Hasegawa, M., Arai, T., Nonaka, T., Kametani, F., Yoshida, M., Hashizume, Y., Beach, T.G., Buratti, E., Baralle, F., Morita, M., et al. (2008). Phosphorylated TDP-43 in frontotemporal lobar degeneration and amyotrophic lateral sclerosis. Ann. Neurol. *64*, 60–70.

Hu, G., Li, H., Liu, J.Y., and Wang, J. (2014). Insight into conformational change for 14-3-3sigma protein by molecular dynamics simulation. Int. J. Mol. Sci. *15*, 2794–2810.

Huang, Q., Chang, J., Cheung, M.K., Nong, W., Li, L., Lee, M.T., and Kwan, H.S. (2014). Human proteins with target sites of multiple post-translational modification types are more prone to be involved in disease. J. Proteome Res. *13*, 2735–2748.

Jacobs, E.J., Newton, C.C., Gapstur, S.M., and Thun, M.J. (2012). Daily aspirin use and cancer mortality in a large US cohort. J. Natl. Cancer Inst. *104*, 1208–1217.

Jacomy, M., Venturini, T., Heymann, S., and Bastian, M. (2014). ForceAtlas2, a continuous graph layout algorithm for handy network visualization designed for the Gephi software. PLoS one *9*, e98679.

Jnoff, E., Albrecht, C., Barker, J.J., Barker, O., Beaumont, E., Bromidge, S., Brookfield, F., Brooks, M., Bubert, C., Ceska, T., et al. (2014). Binding mode and structure-activity relationships around direct inhibitors of the Nrf2-Keap1 complex. Chem. Med. Chem. *9*, 699–705.

Jovanovic, K., Loos, B., Da Costa Dias, B., Penny, C., and Weiss, S.F. (2014). High resolution imaging study of interactions between the 37 kDa/67 kDa laminin receptor and APP, beta-secretase and gamma-secretase in Alzheimer's disease. PLoS One *9*, e100373.

Kamath, R.S., and Ahringer, J. (2003). Genome-wide RNAi screening in *Caenorhabditis elegans*. Methods *30*, 313–321.

Karve, T.M., and Cheema, A.K. (2011). Small changes, huge impact: the role of protein posttranslational modifications in cellular homeostasis and disease. J. Amino Acids *2011*, 207691.

Khaidakov, M., Szwedo, J., Mitra, S., Ayyadevara, S., Dobretsov, M., Lu, J., and Mehta, J.L. (2010). Antiangiogenic and antimitotic effects of aspirin in hypoxia-reoxygenation modulation of the LOX-1-NADPH oxidase axis as a potential mechanism. J. Cardiovasc. Pharmacol. *56*, 635–641.

Kiaei, M., Balasubramaniam, M., Govind Kumar, V., Shmookler Reis, R.J., Moradi, M., and Varughese, K.I. (2018). ALS-causing mutations in profilin-1 alter its conformational dynamics: a computational approach to explain propensity for aggregation. Sci. Rep. *8*, 13102.

Latapy, M., Magnien, C., and del Vecchio, N. (2008). Basic notions for the analysis of large two-mode networks. Social Networks *30*, 31–48.

Lawyer, G. (2015). Understanding the influence of all nodes in a network. Sci. Rep. *5*, 8665.

Lee, S., Xue, Y., Hu, J., Wang, Y., Liu, X., Demeler, B., and Ha, Y. (2011). The E2 domains of APP and APLP1 share a conserved mode of dimerization. Biochemistry *50*, 5453–5464.

Martin, I., Kim, J.W., Lee, B.D., Kang, H.C., Xu, J.C., Jia, H., Stankowski, J., Kim, M.S., Zhong, J., Kumar, M., et al. (2014). Ribosomal protein S15 phosphorylation mediates LRRK2 neurodegeneration in Parkinson's disease. Cell *157*, 472–485.

McFarland, M.A., Ellis, C.E., Markey, S.P., and Nussbaum, R.L. (2008). Proteomics analysis identifies phosphorylation-dependent alpha-synuclein protein interactions. Mol. Cell. Proteomics *7*, 2123–2137.

Moafian, Z., Khoshaman, K., Oryan, A., Kurganov, B.I., and Yousefi, R. (2016). Protective effects of acetylation on the pathological reactions of the

lens crystallins with homocysteine thiolactone. PLoS One *11*, e0164139.

Nagy, Z., Esiri, M.M., and Smith, A.D. (1997). Expression of cell division markers in the hippocampus in Alzheimer's disease and other neurodegenerative conditions. Acta Neuropathol. *93*, 294–300.

Pahrudin Arrozi, A., Shukri, S.N.S., Wan Ngah, W.Z., Mohd Yusof, Y.A., Ahmad Damanhuri, M.H., and Makpol, S. (2017). Evaluation of the expression of Amyloid Precursor Protein and the ratio of secreted Amyloid Beta 42 to Amyloid Beta 40 in SH-SY5Y cells stably transfected with wild-type, single-mutant and double-mutant forms of the APP gene for the study of Alzheimer's disease pathology. Appl. Biochem. Biotechnol. *183*, 853–866.

Petta, I., Lievens, S., Libert, C., Tavernier, J., and De Bosscher, K. (2016). Modulation of protein-protein interactions for the development of novel therapeutics. Mol. Ther. *24*, 707–718.

Ren, Q.G., Liao, X.M., Chen, X.Q., Liu, G.P., and Wang, J.Z. (2007). Effects of tau phosphorylation on proteasome activity. FEBS Lett. *581*, 1521–1528.

Rodriguez-Martin, T., Cuchillo-Ibanez, I., Noble, W., Nyenya, F., Anderton, B.H., and Hanger, D.P. (2013). Tau phosphorylation affects its axonal transport and degradation. Neurobiol. Aging *34*, 2146–2157.

Salama, M., Shalash, A., Magdy, A., Makar, M., Roushdy, T., Elbalkimy, M., Elrassas, H., Elkafrawy, P., Mohamed, W., and Abou Donia, M.B. (2018). Tubulin and Tau: possible targets for diagnosis of Parkinson's and Alzheimer's diseases. PLoS One *13*, e0196436.

Sethi, M.K., and Zaia, J. (2017). Extracellular matrix proteomics in schizophrenia and Alzheimer's disease. Anal. Bioanal. Chem. *409*, 379–394.

Simic, G., Babic Leko, M., Wray, S., Harrington, C., Delalle, I., Jovanov-Milosevic, N., Bazadona, D., Buee, L., de Silva, R., Di Giovanni, G., et al. (2016).

Tau protein hyperphosphorylation and aggregation in Alzheimer's Disease and other tauopathies, and possible neuroprotective strategies. Biomolecules *6*, 6.

Singh, R.K., Ethayathulla, A.S., Jabeen, T., Sharma, S., Kaur, P., and Singh, T.P. (2005). Aspirin induces its anti-inflammatory effects through its specific binding to phospholipase A2: crystal structure of the complex formed between phospholipase A2 and aspirin at 1.9 angstroms resolution. J. Drug Target *13*, 113–119.

Smith, T.W., and Lippa, C.F. (1995). Ki-67 immunoreactivity in Alzheimer's disease and other neurodegenerative disorders. J. Neuropathol. Exp. Neurol. *54*, 297–303.

Stark, L.A., Reid, K., Sansom, O.J., Din, F.V., Guichard, S., Mayer, I., Jodrell, D.I., Clarke, A.R., and Dunlop, M.G. (2007). Aspirin activates the NF-kappaB signalling pathway and induces apoptosis in intestinal neoplasia in two in vivo models of human colorectal cancer. Carcinogenesis *28*, 968–976.

Supplemental Information

Aggregate Interactome Based on Protein

Cross-linking Interfaces Predicts Drug Targets to

Limit Aggregation in Neurodegenerative Diseases

Meenakshisundaram Balasubramaniam, Srinivas Ayyadevara, Akshatha Ganne, Samuel Kakraba, Narsimha Reddy Penthala, Xiuxia Du, Peter A. Crooks, Sue T. Griffin, and Robert J. Shmookler Reis

Figure S1

A RNAi Knockdowns of Random Targets

B

C PCA1, PCA2, PCA3

D Predicted node variables

Figure S2

A

Node Diameter ◯——○
154   1
Interactions
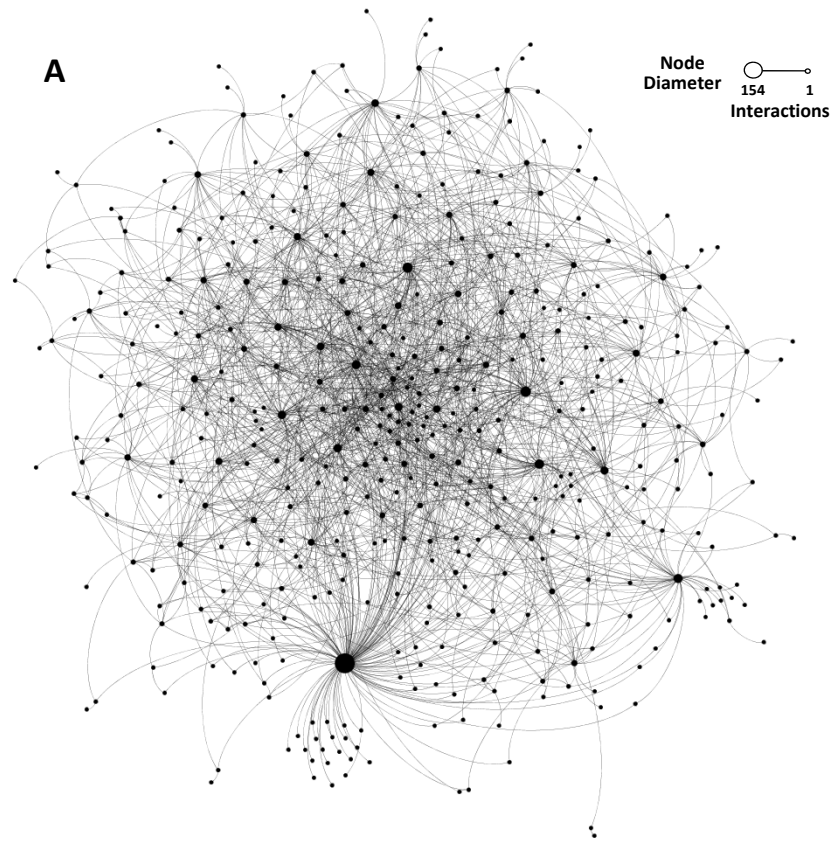
Without ASA treatment: Interactions
common between SY5Y and SY5Y-APP$_{Sw}$

B

Node Diameter ◯——○
35   1
Interactions
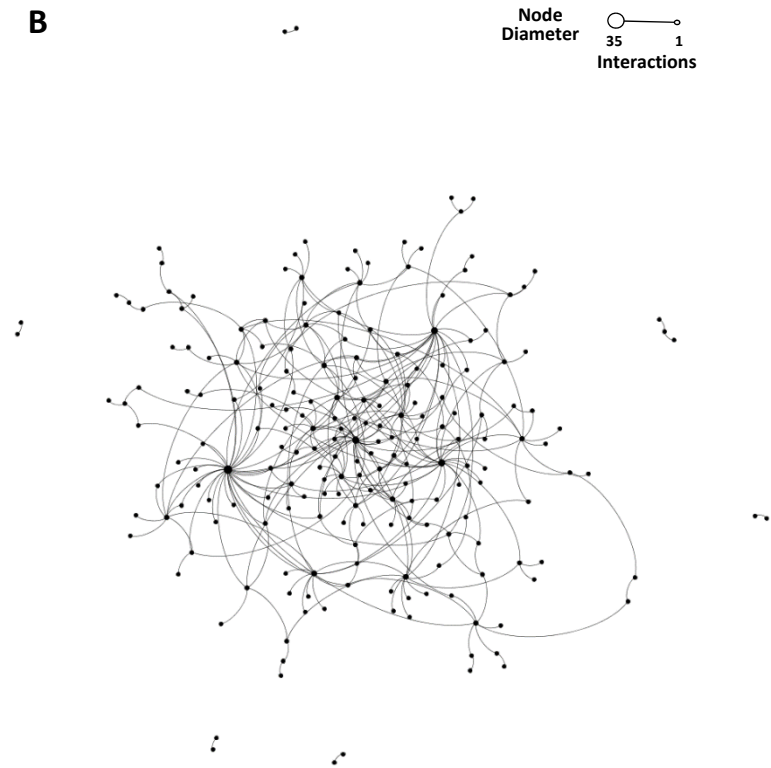
After ASA treatment: Interactions
common between SY5Y and SY5Y-APP$_{Sw}$

Figure S1: Principal components analysis of parameters that predict chemotaxis rescue in a *C. elegans* model of amyloidosis due to leaky neural expression of human Aβ1-42 (related to Figure 4)

(A) Normalized chemotaxis indices of 5-day-old *C. elegans* adults fed 20 random RNAi constructs. Strain CL2355, with leaky [uninduced] pan-neuronal expression of human Aβ42, derived no significant protection against chemotaxis decline, relative to empty-feeding-vector (FV) controls, in marked contrast to the protection conferred when targeting proteins implicated by the aggregate contactome (Figure 4A; of 22 proteins knocked down, 8 gave significant rescue by *t* test, 12 by Chi^2).

(B) Principal Components Analysis (PCA) of the 12 predicted node-protein parameters. Bar height for each orthogonal component shows its contribution to Chemotaxis Index (C.I.) as % of variance explained. Components 1 – 3 account for >90% of total C.I. variance.

(C) Contributions of node variables (X1 – X12) to each of the first 3 principal components. X1=degree (number of interactions); X3 = number of triangles; X4 = Clustering Coefficient; X10 = protein molecular weight.

(D) Cross-correlations among input parameters X1 – X12. Size and shading of circles indicate the strength of positive (blue) or inverse (red) correlation, as indicated by the scale at panel right. Note that degree (X1), Clustering Coefficient (X4), and molecular weight (X10) showed negligible cross-correlation to one another.

Figure S2: **Aggregate contactomes for SY5Y-APP$_{Sw}$ cell aggregates, restricted to protein-protein crosslinks shared in common with SY5Y aggregates (related to Figures 1C and 6C).**

Aggregates were isolated and analyzed exactly as for Figure 1C (corresponding to Figure S2A) and Figure 6C (corresponding to Figure S2B), with the sole additional criterion that interactions were included only if they met the thresholds for both SY5Y-APP$_{Sw}$ and SY5Y aggregates (e.g., black edges in Figure 1C).

(A) Aggregate interactions for untreated SY5Y-APP$_{Sw}$ cells.

(B) Aggregate interactions for SY5Y-APP$_{Sw}$ cells exposed to 0.5-mM aspirin for 48 hours.

Table S1. Parameters that best predict RNAi rescue of declining Chemotaxis Index (C.I.), in a *C. elegans* model of AD-like amyloidopathy (related to Figures 4 and S1)

Protein	Degree	Clustering Coefficient (CC)	Mol.Wt.	Degree x CC	MW x CC	Experimental C.I.	Predicted C.I. (Neural Network)
EIF3A	144	0.14	152.0	19.71	20.80	2.20	2.19
SRSF6	156	0.09	37.8	14.63	3.55	1.72	1.73
RFC1	85	0.21	126.3	17.50	26.00	2.41	2.33
TRIPC	76	0.21	219.1	16.13	46.51	1.56	1.74
SNUT1	91	0.14	88.0	13.00	12.57	1.97	1.76
ZN292	76	0.19	299.5	14.72	58.01	1.87	1.74
ASPM	94	0.10	382.5	9.14	37.19	1.79	1.71
CHD1	66	0.17	98.7	11.45	17.11	1.68	1.63
NUCL	37	0.22	78.1	8.28	17.47	1.53	1.50
DDX52	21	0.30	65.9	6.30	19.77	1.72	1.83
ROA3	12	0.14	41.6	1.64	5.67	2.03	1.88
SF3A3	10	0.22	55.1	2.22	12.25	1.78	1.88
ACTN1	12	0.14	98.1	1.64	13.38	1.98	1.75
RS5	8	0.00	38.7	0.00	0.00	1.72	1.98
DRG1	4	0.00	43.3	0.00	0.00	1.91	2.04
COPG1	4	0.00	96.1	0.00	0.00	2.12	2.03
ANK2	49	0.18	93.6	8.75	16.72	2.21	1.42
CLH1	11	0.44	184.3	4.80	80.40	1.97	2.10
E41L3	13	0.28	119.6	3.67	33.72	1.64	1.88
LAMB	9	0.25	197.8	2.25	49.45	2.64	2.30
LMNA	14	0.36	73.0	5.08	26.49	2.17	2.28
UBA1	11	0.25	41.9	2.80	10.67	1.63	1.90
TAU	13	0.38	83.4	5.00	32.07	2.70	2.45
SERF2	6	0.27	6.9	1.60	1.84	1.92	2.10
PRP8	74	0.14	256.9	10.14	35.18	1.13	1.39
RNPS1	87	0.16	33.6	14.09	5.43	1.67	1.97
PRP4B	140	0.08	110.8	10.66	8.44	1.29	1.31
IF2B	8	0.21	63.5	1.71	13.60	2.33	1.93
TOP2B	57	0.19	178.9	10.86	34.07	1.70	1.40
RBBP6	121	0.13	197.1	16.17	26.34	1.58	1.65
KMT2A	96	0.14	436.6	13.92	63.29	1.73	1.80
NFM	33	0.23	100.8	7.75	23.66	1.31	1.46
EIF3B	7	0.24	89.5	1.67	21.32	1.82	1.97
APP	8	0.32	9.8	2.57	3.15	2.43	2.26
CKAP5	46	0.27	223.5	12.27	59.61	1.70	1.71

C.I. = Fold-change in chemotaxis index upon RNAi knockdown, relative to F.V. controls
The Pearson correlation coefficient between C.I. values observed experimentally, and those predicted by a neural-network algorithm from the above node parameters, was 0.77 ($P<0.0001$).

Transparent Methods

Cell culture and maintenance

Human neuroblastoma cell lines SH-SY5Y and SH-SY5Y-APP$_{Sw}$ (SH-SY5Y cells expressing the "Swedish" familial-AD mutant form of amyloid precursor protein (APP) (Balasubramaniam et al., 2018)), were maintained in culture dishes containing DMEM-F12 (1:1) nutrient mixture (Ham's F-12 Medium) supplemented with 10% v/v fetal bovine serum. Cultures were held at $37 \pm 0.2°C$ with 5% CO_2 in a tissue-culture incubator. Except before and during cross-linking or aspirin treatments, culture media also contained 1% v/v of a penicillin-streptomycin stock (5000 units/ml and 5 mg/ml, respectively; ThermoFisher). For aggregate preparation and cross-linking studies, well-maintained cells were grown to 70% confluence, then detached in trypsin/EDTA, flash frozen under liquid nitrogen in DPBS, and stored at $-80°C$. Aspirin (ASA) was added to SY5Y-APP$_{Sw}$ cells as indicated, at 0.5-mM for 48 h just prior to trypsin digestion and freezing, as detailed above.

Nematode strains and maintenance

C. elegans strain CL2355 [smg-1^{ts} (snb-1/Aβ_{1-42}/long 3'-UTR)], expressing human Aβ_{1-42} in all neurons, serves as a model of Alzheimer-like amyloidosis. CL2355 was obtained from the Caenorhabditis Genetics Center (CGC), stored as frozen larval cultures at $-70°C$, and once thawed, maintained at $20°C$ on solid nematode growth medium (NGM) overlaid with *E. coli* (strain OP50). For gene knockdown, worms (well-fed for ≥ 2 generations) were lysed on day 3 post-hatch and eggs were placed on plates with lawns of *E. coli* expressing RNA-interference constructs from the Ahringer library (Kamath and Ahringer, 2003).

Synthesis of crosslinker-1 (Cross-linking reagent):

Nitromethyltrispropionic acid (**1**, 0.50 g, 1 eq. 1.80 mmol), *N*-(3-dimethylaminopropyl)-*N'*-ethylcarbodiimide hydrochloride (EDC, 1.10 g, 3.2 meq., 5.7 mmol) and *N, N*-diisopropyl-ethylamine (1 mL, 3.2 eq., 5.7 mmol) were added to dry dioxane (10 mL) at 20-25°C under an argon atmosphere. The stirred reaction mixture was heated at 20-25°C for 10 min followed by the addition of *N*-hydroxysuccinimide (**2**, 0.64 g, 3.1 eq., 5.56 mmol). The reaction mixture was stirred for 24 hr or until completion of the reaction (monitored by thin-layer silica-gel chromatography; 100% ethyl acetate mobile phase, product visualization with potassium permanganate spray; R$_f$ = 0.9). After completion of reaction, the mixture was concentrated under gradually reduced pressure

(400 to 30 mm Hg) at 40°C to remove dioxane. The residue was dissolved in ethyl acetate (50 mL), washed with water (2x20 mL), and the separated ethyl acetate layer dried over anhydrous sodium sulfate, filtered and concentrated under reduced pressure to remove the ethyl acetate. The resulting product was precipitated from diethyl ether, filtered, and dried under vacuum to afford compound **3** (Yield: 91%, 0.93 g).

The above tri-NHS ester of nitromethyltrispropionic acid (**3**, 0.90 g, 1 eq., 1.58 mmol) was suspended in a stirred, dry chloroform solution containing propargylamine (**4**, 0.1 mL, 1 eq., 1.58 mmol) under a nitrogen atmosphere at 20-25 °C for 12 hrs. The reaction mass was concentrated by removal of chloroform under gradually reduced pressure (400 → 100 mm Hg) and the resulting residue was extracted into ethyl acetate and washed with ice-cold water (2x10 mL). The separated ethyl acetate layer was washed twice with 1-M phosphate buffer, pH 7.0, and dried over anhydrous sodium sulfate, filtered, and concentrated under reduced pressure to remove the ethyl acetate. The resulting residue was not purified through a silica gel column, because it was previously reported that crosslinker-1 (**5**) undergoes hydrolysis during silica gel chromatography. The residue was dried under vacuum to obtain the crude crosslinker-1 (**5,** Yield: 65%, 0.52 g, ~90% pure from NMR analysis). The NMR spectral data (^{1}H and ^{13}C spectra) were consistent with the reported NMR values (Chowdhury et al., 2009).

Synthesis of crosslinker-2 (cross-linking enrichment reagent):

Biotin (**6**, 1g, 1 eq., 4.09 mmol) was dissolved in dimethyl formamide (DMF; 5 mL), and *N*-(3-dimethylaminopropyl)-*N'*-ethylcarbodiimide hydrochloride (EDC, 0.94 g, 1.2 eq., 4.91 mmol) and *N*, *N*-diisopropylethylamine (0.79 mL, 1.3 eq., 5.32 mmol) added under an argon atmosphere at 20–25°C. The mixture was stirred 10 min prior to addition of *N*-hydroxysuccinimide (**2**, 0.47 g, 1.0 eq., 4.09 mmol). The reaction mixture was then stirred for 24 hrs at 20–25°C and progress of the reaction was monitored by thin-layer silica gel chromatography. After reaction completion, the products were concentrated under reduced pressure to remove DMF. Isopropyl alcohol (50 mL) was then added and the mixture stirred for 10 minutes to form a white precipitate, which was filtered and dried under vacuum to afford compound **7** (Yield: 93%, 1.29 g). The NMR spectral data (^{1}H and ^{13}C-spectra) for compound **7** were consistent with the reported NMR values (Kang et al., 2009) .

NHS-biotin (0.30 g, 1 eq., 0.87 mmol) was added to a dichloromethane (5 mL) solution of 11-azido-3,6,9-undecanamine (**8**, 0.19 g, 1 eq., 0.87 mmol) under nitrogen, and a catalytic amount of triethylamine was added. The resulting reaction mixture was stirred for 12 hr at room temperature under nitrogen and monitored by thin-layer silica-gel chromatography (with 8% MeOH in dichloromethane as solvent). After completion of the reaction, the mixture was washed with water (2x5 mL), and the separated organic layers combined and dried over anhydrous sodium sulfate, filtered and evaporated to dryness to afford crosslinker-2 (**9**, yield: 80%, 0.31 g). Compound **9** was characterized by ^{1}H, ^{13}C-NMR and mass spectra. The NMR spectral data of compound **9** were consistent with the reported NMR values (Li and Zuilhof, 2012; Wang et al., 2009).
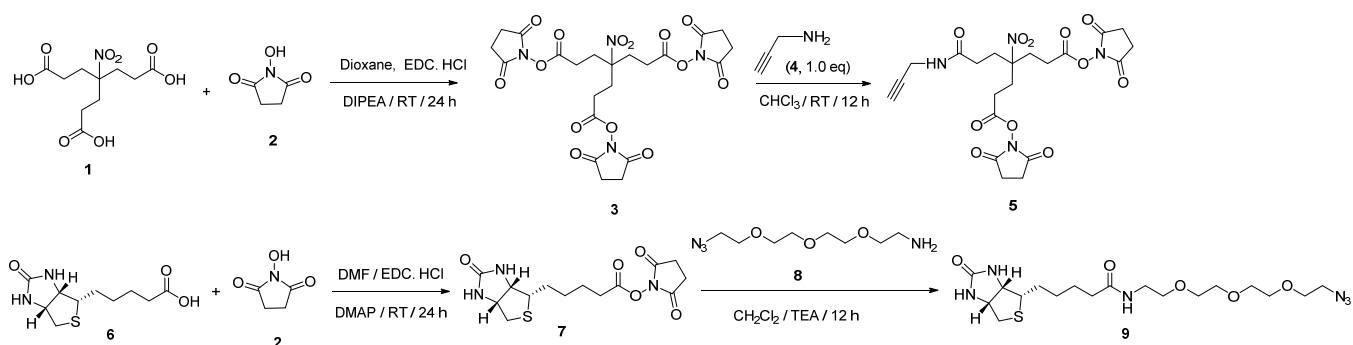
Purification of insoluble aggregates

Frozen cells (SY5Y, SY5Y-APPSw, and SY5Y-APPSw treated with ASA) were pulverized in a Kontes homogenizer, cooled on dry ice. Cell lysis buffer containing inhibitors of proteases and phosphatases was added to crushed, frozen cells as described (Ayyadevara et al., 2017). Cell debris was removed by a brief low-speed centrifugation (5 min, ~1800 g), and total protein was assayed with Bradford reagent (Bio-Rad). Equal protein contents were taken and total aggregates were separated from cytosol by a medium-speed centrifugation (18 min, 18000 rpm). Supernatant (cytosolic fraction) was carefully discarded, and 1% v/v sarcosyl buffer was added to the pellet (total aggregate fractions), as described (Ayyadevara et al., 2017), and incubated for 20 mins at 4°C with gentle shaking. Detergent-insoluble fractions were recovered by high-speed centrifugation (30 min, 90,000 g) and further processed for cross-linking.

Chemical cross-linking of insoluble aggregates

The procedure of Chowdary et al. (Chowdhury et al., 2009) was modified for click-labelling of aggregate proteins and peptide-pair enrichment. Cross-linking reagent propargyl amine was prepared in DMSO, a final concentration of 5uM was added to the insoluble fractions in 20-mM PBS (pH 7.5), and incubated for 30 min at room temperature. The reaction was quenched with 50-mM Tris-HCl (pH 8.0) and cross-linked samples were centrifuged 30 min at 90,000 x g, 4°C, to remove excess unbound cross-linker (in the supernatant).

Tryptic digestion of cross-linked aggregates

Cross-linked aggregates were incubated in buffer containing 8M urea and 122mM DTT,for 30 min at 37°C., followed by a 20 min incubation in dark at 22°C in the presence of 40mM iodo-acetamide. To the reduced sample of protein aggregates 10 units of trypsin (pierce) was added along with 150mM ammonium bicarbonate and incubated overnight at 37°C. Reaction was then quenched by addition of 3% glacial acetic acid.

Isolation of crosslinked peptides

The tryptic peptides are desalted using 1cc C18 column (Sep-Pak, Waters) containing 50mg of resin. Recovered peptide fractions were evaporated to dryness (Speed-Vac, ThermoFisher) and reconstituted in biotin crosslinker containing 0.25-mM TBTA (Tris [(1-benzyl-1H-1,2,3-triazol-4-yl) methyl]amine, 250uM $CuSO_4$, 5-mM Tris-phosphine buffer, and 1:10 molar ratio of biotin crosslinker azide solution and incubated at 4^0 C for 2 hours to facilitate alkyne azide cycloaddition. Biotin attached Crosslinked peptides were isolated with streptavidin coated magnetic beads according to manufacturer's instructions (ThermoFisher)Streptavidin bound peptides were eluted in buffer containing 50% acetonitrile and 0.4 % Tri-Fluro Acetic acid after brief washes with PBS.

LC-MS/MS analysis of cross-linked peptides

Tryptic peptides were separated on a reverse-phase C18 column (120 x 0.075 mm, particle size 2.5μm; Waters XSelect CSH) utilizing an UltiMate 3000 RSLCnano liquid chromatography system (Thermo). Peptides were eluted over a 30 min gradient from 97:3 to 67:33 buffer (A:B ratios, where buffer A contains 0.5% acetonitrile, 0.1% formic acid in LCMS-grade water, and buffer B contains 0.1% formic acid in LCMS-grade acetonitrile). Eluted peptides were ionized by

electrospray (2.15 kV) prior to mass spectrometric analysis on an Orbitrap Fusion Tribrid mass spectrometer (Thermo). MS data were acquired using the FTMS analyzer in top-speed profile mode at a resolution of 4 parts per million over a range of 375 – 1500 m/z. Following CID activation with normalized collision energy of 35.0, MS/MS data were acquired for each peptide using the ion-trap analyzer in centroid mode with three sequential activation settings: HCD activation with normalized collision energy of 28.0, ETD activation with calibrated charge-dependent parameters, and EThcD supplemental activation.

Mass-spectrometry data analysis

Cross-linked peptides from LC-MS/MS spectra were analyzed using Xlink-Identifier(Du et al., 2011). Because the original Xlink-Identifier software does not support parallel processing of data, we developed a Linux-based, in-house script to partition the data and route them to 32 CPUs in parallel for Xlink-Identifier screening. Prior to running Xlink-Identifier, the list of proteins to be considered as potential contributors of crosslinked peptides (the reference database) was compiled from a proteomic analysis of sarcosyl-insoluble aggregates from SY5Y and SY5Y-APP$_{Sw}$ cells, as described previously (Ayyadevara et al., 2017). Only proteins with ≥ 3 spectral hits were included in the reference database used for Xlink-Identifier analysis. To eliminate minor and irreproducible linkages, we incorporated two stringent criteria: (i.) an interlinked peptide should have ≥ 10 spectral hits, and (ii.) the observed protein-protein pair must be present in at least 2 of 3 cross-linking experiments. All data analyses were performed using in-house Linux shell scripts.

Modeling of protein-interaction networks

Results from Xlink-Identifier data analysis were processed by GePhi[TM] (Bastian et al., 2009) and Orange[TM] (Demsar et al., 2013) software packages to model and visualize, respectively, the aggregate interactome. To define characteristic parameters (predictors) for each node, including degree (number of interacting partners) and eigenvector centrality, we used a graph-modeling statistical plugin from GePhi and a network module in the Orange package.

Multivariate-linear-regression and neural-network analyses

Principal component analysis (PCA) and stepwise, forward/reverse multivariate linear regression were performed within their respective R modules. PCA identifies orthogonal input-parameter clusters to collapse highly correlated predictors into a minimal number of uncorrelated predictor

dimensions computed from network graphs for the nodes of interest. Conventionally, PCA (the prcomp function in R) centers the molecular descriptors to have means of zero; we also normalized the variables to have standard deviations of 1. PCA applies linear transformations to fit the 13 predictors into a coordinate system in which the most significant variance is found on the first coordinate (PC1), and each successive coordinate is orthogonal to all others and accounts for a smaller fraction (%) of total variance (R Core Team, 2013). The first three PCs accounted for 75.4%, 8.5%, and 6.4%, respectively, of the total variation in the dataset, thus together explaining >90% of total variance. Even in 2 dimensions, the data provide a close approximation to the original resolution of groups in 13-dimensional space.

The input variables that contributed substantially to PC1 – PC3 were used to build a stepwise, forward-backward multi-variate linear regression (F/R-MLR) model. Model fitting utilized the Akaike information criterion to evaluate the impacts of stepwise additions and removals of independent variables in the model using "stepAIC" and "lm" functions in R (Zeileis et al., 2002). MLR models included 3 individual parameters and all possible combinations of interaction terms (totaling 8 variables) as predictor variables. Data were randomly partitioned (70/30) into training and testing sets. A leave-one-out protocol was also employed for cross-validation of the top-ranked model, to determine the adjusted percent of variance explained by the correlation between predicted and actual chemotactic index (C.I.). After stepwise addition and subtraction, the final model consisted of 3 independent variables and 2 interactions (between degree and MW, and CC and MW), with fold-change in chemotaxis as the dependent variable or prediction target.

We selected the MLR model with the lowest root-mean-square deviation from a linear regression (0.3), requiring $P < 0.001$, to define inputs for neural-network prediction ─ which is inherently both nonlinear and nonparametric.

For neural network training and predictions, we employed a multilayer perceptron (MLP) algorithm with back-propagation, implemented as an Orange^{TM} module (Demsar et al., 2013). The same dataset used for MLR prediction of the chemotaxis index was again randomly split 70:30 into training and testing sets, over 50 iterations. Our neural network algorithm utilized 100 neurons per hidden layer, the activation method was set to ReLu, and solver was selected as Adam (Demsar et al., 2013). RMSE for the neural-network training was 0.4. At the conclusion of the learning and testing iterations, the chemotaxis index (normalized as fold change) was predicted and plotted for the full dataset.

Chemotaxis assay

Chemotaxis was assessed in strain CL2355 (pan-neuronal expression of $A\beta_{1-42}$) as previously described (Ayyadevara et al., 2015). Briefly, eggs from age-synchronized cohorts of worms were fed from hatch with either empty feeding vector (FV) with or without ASA, or with bacteria carrying a plasmid that transcribes complementary exonic RNA strands to direct RNA interference against the gene of interest (Ayyadevara et al., 2015; Kamath and Ahringer, 2003). Worms were maintained at 20°C without acute induction but exhibiting age-dependent loss of chemotaxis (Ayyadevara et al., 2015). ASA stock solution was 100 mM in 95% (v/v) ethanol; prior to each treatment it was diluted to 1 mM in nematode growth medium (NGM). Worms from day 5 (post-hatch) were collected after serial washes to remove any bacteria, and were assayed as previously described (Ayyadevara et al., 2017) in 100 mm culture dishes. Chemotaxis toward 1-butanol was scored after 2 hours and the 'Chemotaxis Index' (CI) was calculated as a normalized response.

Thioflavin-T staining of SY5Y-APP$_{Sw}$ cells

To assess amyloid-like aggregates, SY5Y (wild-type) and SY5Y-APP$_{Sw}$ were stained using thioflavin-T as described previously (Balasubramaniam et al., 2018). Briefly, cells at 70–80% confluence were detached in trypsin/EDTA and sub-cultured in 4-chamber slides (10,000–15,000 cells/chamber) containing antibiotic-free DMEM medium with 10% FBS (Invitrogen). SY5Y-APP$_{Sw}$ cells were treated with 0.5-mM ASA or vehicle alone, and maintained at 37°C for 48 hours. Cells were then fixed (4% v/v formaldehyde), and then incubated with 0.1% (w/v) thioflavin T in phosphate-buffered saline (PBS) along with DAPI. Fluorescence intensities of images captured on a Nikon Eclipse *Ti* microscope were quantified using in-house FIJI (imageJ) scripts.

Protein-protein and protein-ligand docking

The structures of proteins featured in **Figure 2, C&D,** were obtained from PDB (Protein DataBase). Proteins represented in **Figure 6, F-J,** were modelled in 3 dimensions using Modeller (by homology modeling) or fold recognition and *ab-initio* methods (implemented by the iTASSER server) (Yang and Zhang, 2015), with the exception of controls in **Figure 6F**, for which structures were obtained from PDB. Protein-protein docking was modeled by the Hex 6.1 program, based on shape and electrostatic charge complementarity as previously described (Balasubramaniam et al., 2018; Ritchie et al., 2008), with other docking parameters set to default. To analyze ASA

interactions, protein-ligand docking was implemented in AutoDock-Vina (Linux based) using the Raccoon (Windows) interface. The lowest docking-energy ($\Delta G_{binding}$) pose was taken as the best model. Results were analyzed and plotted using the Discovery Studio visualizer (BIOVIA, Dassault Systemes, San Diego [2017])

Statistical analyses

We compared groups of replicate samples by 2-tailed *t* tests if group size was >10 (e.g., **Figures 1B and 6B**), or Behrens-Fisher (heteroscedastic) *t* tests for smaller samples in which variance was unknown or may be unequal. In some instances, when the direction of change is known or strongly predicted, a 1-tailed *t* test may be substituted. Differences in proportions were assessed within an experiment by Chi-squared (Chi^2) or Fisher Exact tests (e.g., asterisks in **Figure 4A**). If replication is sufficient, ratios from individual experiments may be treated as points within groups, which can then be compared by heteroscedastic *t* tests (e.g., numbers above bars in **Figure 4A**).

In experiments with multiple end-points, Bonferroni corrections have not been applied, leaving it to the reader to compare the frequency of "positives" to their expected frequency (e.g., 5% at α = 0.05).

Network parameters

Two of the standard descriptors used widely to characterize local network properties are the Clustering Coefficient (CC), by which we here mean the local, undirected clustering coefficient, as the fraction of triplets (potential node-triangles) directly connected to that node, that form closed triangles of 3 interconnected nodes [51]. For any vertex v_i (node *i* with at least 2 interacting partners), CC_i is calculated as $C_i = \frac{2|\{e_{jk} : v_j, v_k \in N_i, e_{jk} \in E\}|}{k_i(k_i - 1)}$ where v_j and v_k are vertices directly connected to v_i (Watts and Strogatz, 1998). Eigenvector centrality (EC) reflects node connectivity to high-degree hubs, comprising both direct and indirect connectivity. EC is calculated as $x_v = \frac{1}{\lambda} \sum_{t \in M(v)} x_t = \frac{1}{\lambda} \sum_{t \in G} a_{v,t} x_t$ where $M(v)$ is the set of the neighbors of vertex *v,* and λ is a constant (https://gephi.org). Highly influential hub connectors are those for which CC/EC $\leq$100, using normalized EC values (Watts and Strogatz, 1998).